A&A 648, A64 (2021)
https://doi.org/10.1051/0004-6361/202039896

Astronomy & Astrophysics

Star formation quenching stages of active and non-active galaxies

V. Kalinova[1], D. Colombo[1], S. F. Sánchez[2], K. Kodaira[1,3,4], R. García-Benito[5], R. González Delgado[5], E. Rosolowsky[6], and E. A. D. Lacerda[2]

[1] Max Planck Institute for Radioastronomy, Auf dem Hügel 69, 53121 Bonn, Germany
e-mail: kalinova@mpifr.de
[2] Instituto de Astronomía, Universidad Nacional Autonóma de México, A.P. 70-264, 04510 Mexico DF, Mexico
[3] National Astronomical Observatory of Japan, Osawa2-21-1, Mitaka-shi, 181-8588 Tokyo, Japan
[4] SOKENDAI, International Village, Hayama-machi, Miura-gun 240-0193, Kanagawa-ken, Japan
[5] Instituto de Astrofísica de Andalucía, CSIC, Apartado de correos 3004, 18080 Granada, Spain
[6] Department of Physics 4-181 CCIS, University of Alberta, Edmonton, AB T6G 2E1, Canada

Received 12 November 2020 / Accepted 21 January 2021

ABSTRACT

The mechanisms that bring galaxies to strongly reduce their star formation activity (star-formation quenching) remain poorly understood. To better study galaxy evolution, we propose a classification based on maps of ionised hydrogen distribution traced by the kiloparsec-resolved, equivalent width of Hα maps, and the nuclear activity of the galaxies using information from the Baldwin-Philips-Terlevich diagnostic diagrams. Using these tools, we group a sample of 238 galaxies from the Calar Alto Legacy Integral Field spectroscopy Area survey in six quenching stages (QSs): (i) objects dominated by recent star formation; (ii) systems that present a quiescent-nuclear-ring structure in their centre; (iii) galaxies that are centrally quiescent; (iv) galaxies with no clear pattern in their ionisation gas distribution (mixed); (v) systems that posses only a few star-forming regions (nearly retired), or (vi) galaxies that are completely quiescent (fully retired). Regarding their nuclear activity, we further divide the galaxies into two groups: active systems that host a weak or strong active galactic nucleus (AGN) at their centre, and non-active objects. Galaxies grouped into quenching-stage classes occupy specific locations on the star-formation-rate versus stellar mass diagram. The 'blue cloud' is populated by the star-forming and the quiescent-nuclear-ring galaxies, the 'green valley' is populated by centrally quiescent and mixed systems, and the 'red sequence' by the nearly- and fully retired objects. Generally, galaxies that host a weak or strong AGN show properties comparable to those of their non-active counterparts at the same QSs, except for the AGN-hosting star-forming systems. The degree of star-formation quenching increases along the present emission-line pattern sequence from star-forming to fully retired. The proposed emission-line classes reinforce the 'inside-out' quenching scenario, which foresees that the suppression of star formation begins from the central regions of the galaxies.

Key words. galaxies: evolution – galaxies: structure – galaxies: star formation – galaxies: active – galaxies: nuclei – galaxies: fundamental parameters

1. Introduction

Distributions of galaxy properties such as morphologies (Hubble 1926), colours (Strateva et al. 2001; Baldry et al. 2004), star-formation rates (SFRs; Brinchmann et al. 2004; Renzini & Peng 2015), ages (Gallazzi et al. 2005, 2008; Zibetti et al. 2017), and gas content (e.g. Young & Scoville 1991; Blanton & Moustakas 2009) in the local universe show strong bi-modality. Similar bi-modality is observed even up to $z \sim 2.5$ (Brammer et al. 2009; Williams et al. 2009). The so-called red sequence is populated by red spheroidal systems, while the blue cloud hosts blue disc galaxies. The region in between is called the green valley and is underpopulated, suggesting that the transition occurs within a narrow range of certain galaxy parameters from the blue cloud to the red sequence. Galaxies in the green valley do not show a particular morphology (Schawinski et al. 2014) or other particular properties, rather their colour is the consequence of the switching off of star formation, a process usually referred to as star formation quenching (e.g. Faber et al. 2007). Indeed, when posed on an SFR versus stellar mass (M_*) diagram, galaxies show the same bi-modality, with star-forming galaxies tightly organised across the star formation main sequence (SFMS, e.g. Brinchmann et al. 2004; Whitaker et al. 2012; Renzini & Peng 2015; Speagle et al. 2014; Cano-Díaz et al. 2016; Sánchez et al. 2019), retired galaxies in the corresponding red sequence, and galaxies in the process of quenching (immediately below the SFMS) in the green valley (e.g. Schawinski et al. 2014).

The integrated SFR versus M_* diagram (SFR-M_*) has been broadly explored in the literature (e.g. Schawinski et al. 2014; Renzini & Peng 2015; Catalán-Torrecilla et al. 2015, 2017; González Delgado et al. 2016; Cano-Díaz et al. 2016, 2019; Belfiore et al. 2018; Bluck et al. 2019; Sánchez et al. 2018, 2019; Lacerda et al. 2020) and has served as an important diagnostic tool for studying galaxy evolution.

Additionally, galaxy evolution theories have been largely constrained through ionised gas emission-line (EL) classification schemes that study the star formation, chemical properties, and nuclear activity of large samples of galaxies. Baldwin et al. (1981; see also Veilleux & Osterbrock 1987) originally proposed a diagram (now known as the Baldwin-Philips-Terlevich (BPT) diagram) that uses the intensity ratio of emission lines ([O III] λ5007/Hβ versus [N II] λ6584/Hα line ratios) to distinguish between dominant excitation sources (such as HII regions, power-law continuum spectrum photo-ionisations, and heating by shock waves in the original formulation) from the spectra of extragalactic objects. Later on, Kauffmann et al. (2003) defined

loci on the BPT diagram to distinguish star-forming and starburst galaxies (see also Kewley et al. 2001), Seyfert regions related to galaxies hosting an active galactic nucleus (AGN), or low-ionisation nuclear emission regions (LINERs), in which the ionisation might be attributed to old and hot stars (e.g. Stasińska et al. 2008).

More recently, Cid Fernandes et al. (2011) proposed a different bi-dimensional diagram to disentangle the excitation source in the centre of galaxies: The 'WHAN' diagram considers the equivalent width of the Hα ($W_{\rm H\alpha}$) versus the [N II] λ6584/Hα ratio to classify galaxies into purely star-forming or strong AGN hosts. Additionally, this diagnostic is able to distinguish between objects that are retired (or passive) and galaxies that genuinely host a weak AGN.

The advent of spatially resolved integral field spectroscopy (IFS) surveys such as ATLAS^{3D} (Cappellari et al. 2011), Calar Alto Legacy Integral Field spectroscopy Area (CALIFA; Sánchez et al. 2012), Sydney-AAO Multi-object Integral field spectrograph (SAMI; Croom et al. 2012), Mapping Nearby Galaxies at Apache Point Observatory (MaNGA; Bundy et al. 2015), and All-weather MUse Supernova Integral field Nearby Galaxies (AMUSING++; López-Cobá et al. 2020) has provided large statistical samples with which to study excitation sources of the ionised gas not only between galaxies, but also within them. In particular, they enable identification of the dominant excitation source of a galaxy, because different galactic regions can be characterised by a large variety of ionisation effects (see Sánchez 2020 for an extensive review).

An attempt to classify single regions of galaxies through the use of the BPT diagram was made by Singh et al. (2013), who show that excitation properties that characterise LINERs are not simply limited to the nuclear regions, but extend far away from the galactic centre. Those 'low ionisation emission regions' (therefore redefined as 'LIERs') are probably due to post-AGB stars rather than to AGN activity. Following a similar method, Belfiore et al. (2016) used the BPT scheme to group galaxies based on their dominant excitation source and consider the spatially resolved patterns described by the diagram. This classification distinguishes between galaxies dominated by star formation, galaxies hosting an AGN, objects that show LIERs only in the centre (cLIERs) or throughout their full extent (eLIERs), and mergers. In particular, cLIERs are bulged spiral galaxies located in the green valley, while eLIERs are basically elliptical, retired objects.

The diffuse ionised gas classification proposed by Lacerda et al. (2018) instead put emphasis on the use of resolved $W_{\rm H\alpha}$ maps to show where the gas excitation in the different galaxy regions is powered by hot low-mass evolved stars (HOLMES; Flores-Fajardo et al. 2011), HII regions (and therefore star formation), or a mixture of both effects. This scheme is simple, because it involves the use of $W_{\rm H\alpha}$ only, but effective because its predictions are largely consistent with those based on the BPT diagram. However, it does not aim to put a galaxy in a given category, but rather to classify galactic regions in diffuse ionised gas classes. Furthermore, it does not allow the user to distinguish excitation due to AGNs. Recent works of Sánchez et al. (2018) and Lacerda et al. (2020) define and explore the properties of AGN hosts from large samples of MaNGA and CALIFA galaxies, respectively, through classification based on the information from the BPT diagrams and the $W_{\rm H\alpha}$ values of the central galaxy regions.

In the present article, we synthesise the $W_{\rm H\alpha}$ values and BPT-diagram classification approaches in a similar way in order to propose a new bi-dimensional method that distinguishes between several 'star formation quenching stages', considering the nuclear activity of the galaxy. The novelty of our method is that it not only defines galaxy groups based on the global $W_{\rm H\alpha}$ value or the $W_{\rm H\alpha}$ value at particular radii, but also considers the patterns described by the resolved $W_{\rm H\alpha}$ map across the entire galaxy. Our method is inspired by the previous work of Sánchez et al. (2013), who first proposed the use of the resolved $W_{\rm H\alpha}$ map to distinguish between star-forming and retired regions in the galaxies, extending the selection introduced by the WHAN diagram (see also Sánchez et al. 2014, 2018; Sánchez-Menguiano et al. 2016, 2018; Cano-Díaz et al. 2016, 2019; López-Cobá et al. 2019; Sánchez 2020). The proposed classification compares the properties of active and non-active systems with various ionisation distributions and is used here to investigate the quenching mechanisms that transform galaxies from one type to another.

This study is organised as follows: Sect. 2 describes the sample selection and the analysed data; Sect. 3 defines the criteria of the emission-line classification; and Sects. 4 and 5 present the resolved and global properties of the EL galaxies. Finally, Sects. 6 and 7 present our discussion and summary, respectively.

2. Data and analysis

2.1. Sample selection

Our study is based on CALIFA integral-field unit (IFU) data, which observed 667 galaxies (in its third data release, Sánchez et al. 2016a) in the redshift range $0.005 < z < 0.03$ using the Potsdam Multi-Aperture Spectrophotometer (PMAS, Roth et al. 2005) in PPaK (PMAS fiber Package, Verheijen et al. 2004; Kelz et al. 2006) mode, installed on the 3.5 m telescope at the Calar Alto observatory. In particular, CALIFA targets span various morphologies and stellar masses, forming a representative sample of nearby Universe galaxies. Further details can be found in the survey-presentation paper (Sánchez et al. 2012), the data-release papers (Husemann et al. 2013; García-Benito et al. 2015; Sánchez et al. 2016a), and the sample paper of Walcher et al. (2014).

For this work, we adopt the sample of 238 CALIFA galaxies originally explored in Kalinova et al. (2017a, hereafter K17). This sample was originally selected from Falcón-Barroso et al. (2017), who provided stellar kinematics maps for 300 CALIFA galaxies observed until June 2014. After exclusion of mergers and galaxies with unreliable dynamical models, K17 present a sample of 238 targets in a broad range of stellar masses (from $6 \times 10^8\ M_\odot$ to $5 \times 10^{11}\ M_\odot$) and types (from E1 to Sdm). The current sample is representative of the CALIFA mother sample (see Fig. 1 in K17) and is therefore representative of the local Universe galaxy population too.

2.2. Emission-line data

There are three sets of CALIFA data: low-spectral-resolution mode V500 ($FWHM \sim 6$ Å), high-resolution V1200 ($FWHM \sim 2.3$Å), and a combination of both observation setups, called COMBO data ($FWHM \sim 6$Å). V500 ranges between 3745 and 7500 Å, V1200 between 3650 and 4840 Å, and COMBO between 3700 and 7500 Å (see Sánchez et al. 2016a). Depending on scientific goals, we use different data sets in order to optimise our results. For example, the COMBO dataset has the same resolution as V500, but gives more reliable spectrophotometry at the blue end of its spectra ($\lambda < 4600$ Å), which contains important stellar population tracers (i.e. COMBO data are not influenced

by vignetting effects). For this set of galaxies, we make use of the ionised gas maps of Hα, Hβ, [NII], [SII], [OI], [OIII] line fluxes, and $W_{H\alpha}$ obtained with the Pipe3D pipeline using the low-resolution mode V500 of the CALIFA data set, where the lines are strong and present in this spectral window (in contrast to V1200 data), and available for all galaxies of our sample (in contrast to COMBO data).

Full details about Pipe3D are given in Sánchez et al. (2016c,b); here we provide a short description. The pipeline uses a combination of synthetic simple stellar population (SSP) spectra from the GRANADA library (Martins et al. 2005) and empirical ones from the MILES project (Sánchez-Blázquez et al. 2006; Vazdekis et al. 2010; Falcón-Barroso et al. 2011). This joint SSP-library (see more details in Cid Fernandes et al. 2013) adopts the Salpeter (Salpeter 1955) initial mass function (IMF). It consists of 156 templates, covering 39 stellar ages (from 1 Myr to 14 Gyr), and 4 metallicities ranges ($Z/Z_\odot$ = 0.2, 0.4, 1 and 1.5). The library uses Girardi et al. (2000) evolutionary tracks, except for the youngest ages between 1 Myr and 3 Myr, which are based on Geneva tracks (Schaller et al. 1992; Schaerer et al. 1993a,b; Charbonnel et al. 1993).

The original V-band data-cube is binned to increase the signal-to-noise ratio (S/N) but keep the overlap between regions with different physics to a minimum. A spaxel-wise stellar population fit is performed using Fit3D. Afterwards, the model is evaluated by considering the continuum flux within each spatial bin. The ionised emission line data cube is then constructed by subtracting the stellar-population model spaxel by spaxel. Pipe3D analyses 52 emission lines and provides various maps (e.g. flux intensity, velocity, velocity dispersion and $W_{H\alpha}$), alongside their uncertainties.

2.3. Stellar population data

In order to derive the star-formation history properties of the galaxies and to optimise our results, we rely on the COMBO dataset, which provides a free vignetted field of view (FOV) on the blue side of the spectral range in contrast to V500 alone (although COMBO data are not available for seven galaxies in our sample; see Table B.1). We estimated the stellar surface-mass-density (μ_*), stellar mass (M_*), age (τ), metallicity (Z), and SFR of the galaxies assuming a Chabrier IMF (Chabrier 2003), which is necessary for the comparison of our sample with Sloan Digital Sky Survey (SDSS[1]) reference galaxies in the context of SFR-M* diagram exploration in Sect. 6.1. As PIPE3D only adopts a Salpeter IMF, this makes it inconvenient for our analysis here. We instead run the STARLIGHT spectral synthesis code of Cid Fernandes et al. (2005) on the COMBO data, fitting the individual spectra for each spatially resolved element of the IFU, and then implementing the output results in the platform of Python CALIFA STARLIGHT Synthesis organiser (PyCASSO; de Amorim et al. 2017) to obtain the spatially resolved data.

For the fits, we use the CBe base of Charlot & Bruzual (2007, priv. comm.), which is a combination of 246 single stellar population (SSP) spectra covering 41 ages from 0.001 to 14 Gyr and six metallicity ranges: $\log Z/Z_\odot$ = −2.3, −1.7, −0.7, −0.4, 0, +0.4. The SSP models are revised from Bruzual & Charlot (2003), where both MILES (Sánchez-Blázquez et al. 2006; Falcón-Barroso et al. 2011) and GRANADA (Martins et al. 2005) stellar libraries replace the original library STELIB (Le Borgne et al. 2003). Further, 'Padova 1994' stellar tracks has been applied (Alongi et al. 1993; Bressan et al. 1993; Fagotto et al. 1994a,b,c; Girardi et al. 1996). For more details about the SSP analysis, we refer to the related works of Cid Fernandes et al. (2013), González Delgado et al. (2015), de Amorim et al. (2017), García-Benito et al. (2017, 2019).

The mean stellar surface brightness, μ_*, is extinction corrected and calculated within $1R_e$. The galaxy age (τ) and metallicity (Z) are light- and mass-weighted within $1R_e$, respectively. The total SFR is calculated from the spatially resolved star formation history of galaxies by adding the amount of stellar mass formed into stars in the last 32 Myr (and divided by this time interval; González Delgado et al. 2016, 2017; de Amorim et al. 2017). This approach helps to account for the star formation of the galaxies that is heavily obscured or has a low quantity of ionised gas (i.e. those galaxies where the H_α emission is very weak). The SFR from H_α has a shorter timescale of emission in comparison to the SFR from SSP, which mainly comes from OB stars (3 Myr, Kennicutt & Evans 2012). In addition, the SSP-based approach averages over stochastic star formation to provide a good estimation of the SFR.

2.4. Photometric data

We analysed the photometric properties of our galaxies using SDSS data (Abazajian et al. 2009; Alam et al. 2015). We derived the bulge-to-disc (B/D) ratios of the galaxies from their bulge-to-total (B/T) and disc-to-total (D/T) flux ratios, which are provided by Méndez-Abreu et al. (2017), who analyse r-band SDSS images from Data Release (DR) 7 (Abazajian et al. 2009) of 404 CALIFA galaxies. The overlap with our sample (for galaxies with both available B/T and D/T ratios) is 127 galaxies, which approximately covers half of the galaxies within each EL class, with no significant changes across our classes. Thus, we do not expect large bias in our conclusions regarding B/D ratios.

We calculated the total luminosity (L_r^{tot}) of the galaxies from the r-band SDSS (DR12; Alam et al. 2015) images using the Multi-Gaussian Expansion method (MGE; Emsellem et al. 1994) by K17. We measured the effective radii (R_e) using a growth curve analysis based on elliptical apertures from SDSS DR7 (Abazajian et al. 2009) images, which provide reliable estimations in cases of highly inclined galaxies (Sanchez et al., in prep.). The galaxy morphology and the presence of a bar were defined visually by a few members of the CALIFA team as described in Walcher et al. (2014).

2.5. Kinematical and dynamical data

To calculate the galactic specific angular momentum (λ_{R_e}) of our galaxies, we use the public available stellar kinematic maps of the CALIFA galaxies, provided by Falcón-Barroso et al. (2017). They use the high-resolution V1200 setup of CALIFA data, which has much higher spectral resolution (~72 km s^{-1}) than V500 grating (~139 km s^{-1}), and where V500 has difficulty in reliably measuring velocity dispersions below 100 km s^{-1} (see Sect. 4.2 of their paper). Further, Falcón-Barroso et al. (2017) derive the line-of-sight velocity (V) and velocity dispersion (σ) distributions after fitting the stellar continuum of the galaxies in each spatial bin using the `pPXF` code of Cappellari & Emsellem (2004) with stellar templates from the Indo-US spectral library (Valdes et al. 2004). The averaging of the pixels was done using the Voronoi 2D binning method of Cappellari & Copin (2003) with a minimal S/N of 20 per pixel.

We calculate the specific angular momentum λ_{R_e} using Eq. (6) in Emsellem et al. (2007):

[1] https://www.sdss.org/

$$\lambda_{R_e} = \frac{\sum_{i=0}^{N_k} F_i R_i |V_i|}{\sum_{i=0}^{N_k} F_i R_i \sqrt{V_i^2 + \sigma_i^2}}, \quad (1)$$

where F_i, R_i, V_i and σ_i are the flux, circular radius, velocity, and velocity dispersion of the i-th spatial bin.

We report λ_{R_e} as the integrated value within one effective radius of the galaxy, reached by all of our targets. Our measurements of λ_{R_e} are comparable to the published calculations of Falcón-Barroso et al. (2019), although we adopt different values for the position angles and the inclinations of the galaxies (from K17).

The amplitude ($V_{c,max}$) of the circular velocity curve of the galaxies within $1.5R_e$ is inferred from stellar dynamical modelling (Sect. 3.1 in K17) based on axisymmetric Jeans equations (i.e. using the JAM[2] code of Cappellari 2008). In addition, the total dynamical mass M_{dyn}^{tot} (panel K) comes from multiplication of the total luminosity (L_r^{tot}) derived via the MGE method (Emsellem et al. 1994) by the dynamical mass-to-light ratio γ_{dyn} of the galaxies obtained using the Markov Chain Monte Carlo approach (MCMC; Foreman-Mackey et al. 2013) of the JAM model (see Kalinova et al. 2017b). Our masses are comparable to the recent calculations of the dynamical mass by Aquino-Ortíz et al. (2018), who use the kinematic parameter $S_k^2 = K\,V_{rot}^2 + \sigma^2$ as a dynamical proxy (where K is constant, V_{rot} is the rotation velocity, and σ is the velocity dispersion of the galaxy; Weiner et al. 2006). To calibrate the constant K, Aquino-Ortíz et al. (2018) use the dynamical mass measurements of Leung et al. (2018), Zhu et al. (2018a), and Zhu et al. (2018b).

Through M_{dyn}^{tot} and M_*^{tot}, we calculate the mass discrepancy factor $f_d = 1 - (M_*^{tot}/M_{dyn}^{tot})$, showing the relationship between the total stellar and dynamical masses as a fraction.

3. Two-dimensional emission-line classification

We classify galaxies according to their ionisation, following recent studies in the field (Schawinski et al. 2007; Stasińska et al. 2008; Cid Fernandes et al. 2011; Singh et al. 2013; Belfiore et al. 2016; Sánchez et al. 2018; Sánchez 2020; Lacerda et al. 2020). In particular, our classification is based on the peculiar patterns defined by the spatially resolved Hα-equivalent-width ($W_{H\alpha}$) value within the galaxies (similar to Cid Fernandes et al. 2011; Sánchez et al. 2018; Lacerda et al. 2018, 2020; Espinosa-Ponce et al. 2020). Briefly, star-forming or HII regions show $W_{H\alpha} > 6$ Å; finding $W_{H\alpha} \leq 3$ Å indicates that the gas in the region is ionised by the old stellar population (post-AGB stars or HOLMES); values of $3\,Å < W_{H\alpha} \leq 6$ Å are consistent neither with star formation nor HOLMES, but rather with other mixed phenomena (e.g. diffuse ionised gas, high-velocity shocks; e.g. Lacerda et al. 2018). Therefore the $W_{H\alpha}$ values of 3 Å and 6 Å mark the thresholds we use to recognise patterns in the resolved $W_{H\alpha}$ map (see also Cid Fernandes et al. 2011).

To distinguish between the active and non-active galaxies of our sample (i.e. whether or not they host an AGN in their centres), we use three BPT excitation diagnostic diagrams (and their corresponding maps) involving the [OIII], [SII], [OI], and [NII] line ratios with respect to the Balmer lines (Baldwin et al. 1981, Veilleux & Osterbrock 1987). We assess these diagrams using the loci separating different ionisation regimes proposed by Kauffmann et al. (2003). The utility of combining $W_{H\alpha}$ together with the BPT diagnostic diagrams has been suggested by many authors (e.g. Sarzi et al. 2010; Cid Fernandes et al. 2010; Singh et al. 2013; Sánchez et al. 2014; Lacerda et al. 2018, 2020). Thus, the galaxy is defined as a host of a weak AGN if its central pixels, located within $0.5R_e$ of the galaxy, populate the Seyfert region of the BPT diagrams and their $W_{H\alpha}$ values range between 3 Å and 6 Å. In case the $W_{H\alpha}$ values of those central pixels go above 6 Å, then the galaxy is considered to host a strong AGN (see Sect. 3.2 for more details.)

We apply a 1-σ clipping to the $W_{H\alpha}$ maps and measurements in the BPT diagrams, which removes low-signal-to-noise-ratio spaxels. We experimented with a stricter 3-σ clipping, but this omitted targets with lower S/Ns in the emission-line data (typically for old population galaxies).

Visually identifying dominant patterns in the $W_{H\alpha}$ maps of CALIFA galaxies, we find six quenching stages (QSs): star-forming, quiescent-nuclear-ring, centrally quiescent, mixed, nearly retired, and fully retired. On the other hand, from the BPT diagrams we distinguish three nuclear activities (NAs) of the galaxies: non-active, weak AGN (wAGN), and strong AGN (sAGN).

If we explore the properties of the galaxies only by the QS criteria, we refer to a 'quenching classification', while if we explore the galaxies only through their nuclear activity criteria, we link to a 'nuclear activity classification'. In Fig. 1, we combine both QS and NA criteria and define a two-dimensional (2D) emission-line classification called QuestNA (QUEnching STages and Nuclear Activity).

QuestNA can be expressed as a matrix of six QS rows by three NA columns, giving eighteen EL classes, but in reality the EL classes only show fourteen populated classes, because centrally quiescent and fully retired QSs do not allow a nuclear activity in the centre of the galaxies by definition: the $W_{H\alpha}$ values in these regions are equal to or below 3 Å, which is too low to distinguish the AGN activity from the other processes in the galaxies (e.g. Cid Fernandes et al. 2010; Sánchez et al. 2014; Lacerda et al. 2020). The QS rows are ordered by increasing ratio of retired/star-forming regions in the galaxy, while the NA columns are organised according to the increasing nuclear activity of the galaxy (i.e. non-active→wAGN→sAGN).

3.1. Quenching stage criteria

Based on the distribution of ionisation in different regions within the 238 CALIFA galaxies and visual inspection of their $W_{H\alpha}$ maps, we propose the following QSs of the galaxies (i.e. this is the first dimension of the emission-line classification):

(i) Star-forming galaxies. The first row of panels (A–C) of Fig. 1 exemplifies the typical star-forming class galaxies (NGC 1151, NGC 0214 and NGC 7466) from each type of nuclear activity (non-active, wAGN, and sAGN, respectively). The median value of the $W_{H\alpha}$ spaxels should be larger than 6 Å and there are no large regions in these galaxies with low-ionisation emission lines, where $W_{H\alpha} < 3$ Å (such low ionisation spaxels are usually less than 3% of the total ones). The star-forming class can be represented by both active and non-active galaxies.

(ii) Quiescent-nuclear-ring galaxies. The second row of panels (D–F) of Fig. 1 represents the quiescent-nuclear-ring class galaxies (NGC 3811, NGC 7321 and UGC03995) from each type of nuclear activity. This group is characterised by a quiescent-nuclear-ring region within the $0.2–0.5R_e$ of the galaxy, where the $W_{H\alpha}$ is below 3 Å. On the other hand, the

[2] http://purl.org/cappellari/software

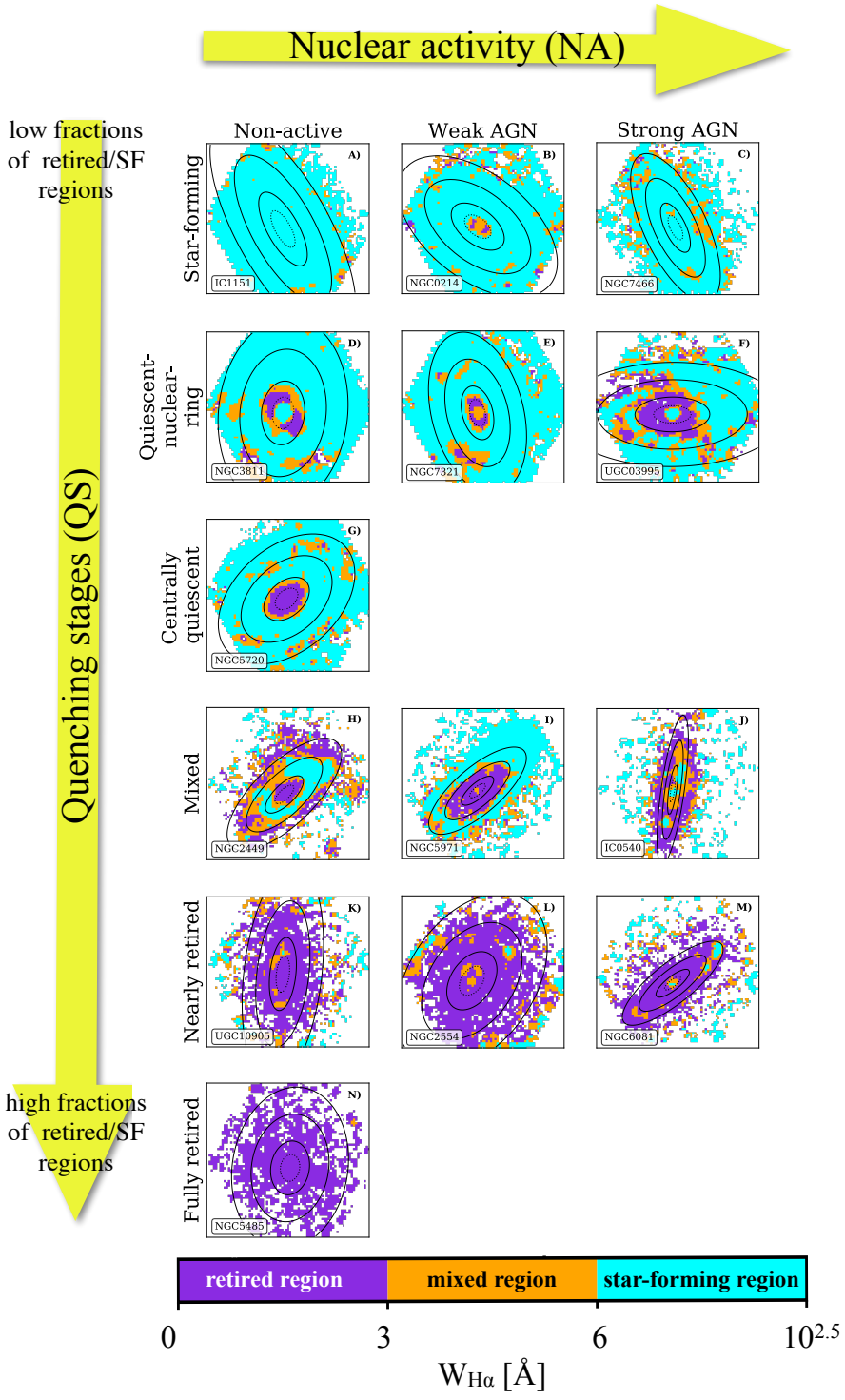

Fig. 1. Two-dimensional emission line classification 'QuestNA' of our sample of galaxies (see Sect. 3). The rows represent the quenching stages of the galaxies: star-forming, quiescent-nuclear-ring, centrally quiescent, mixed, nearly retired, and fully retired with increasing 'retired/star-forming regions' ratio of the galaxy *from top to bottom*. The columns reflect the level of galaxy nuclear activity: non-active, weak, and strong AGN *from left to right*. Each panel of the scheme shows the $W_{H\alpha}$ map of the galaxy, where the dashed contour indicates 0.5 of the effective radius, and the continuous contours correspond to 1, 2, and $3R_e$, respectively. The colour bar of the $W_{H\alpha}$ maps divides the regions of the galaxy into star-forming ($W_{H\alpha} > 6$ Å), retired ($W_{H\alpha} \leq 3$ Å), and mixed (3 Å $< W_{H\alpha} \leq 6$ Å). There are 14 emission-line classes of QuestNA instead of 18, because two of the quenching stages, centrally quiescent and fully retired, are only non-active galaxies, which by definition are fully retired in the central regions.

central spaxels, which are surrounded by the ring, always have $W_{H\alpha}$ values above 3 Å. In the outer regions of the galaxies (0.5–2.0R_e), there is evidence for the presence of a star-forming disc with $W_{H\alpha}$ values going above 6 Å. The quiescent-nuclear-ring class contains both active and non-active galaxies.

(iii) Centrally quiescent galaxies. In panel G of Fig. 1, galaxy NGC 5720 represents the centrally-quiescent class galaxies, which shows low-ionisation EL regions at small galactocentric radii: $W_{H\alpha}$ stays below 3 Å up to 0.5R_e. There is evidence for the presence of a star-forming disc because $W_{H\alpha}$ values go above 6 Å within the range 0.5−2.0R_e. The centrally quiescent class are only non-active galaxies because the $W_{H\alpha}$ value of the central pixels is always equal to or below 3 Å even in cases where the line ratios populate the Seyfert region of the BPT diagrams. This class is similar to the cLIER galaxies from the [SII]-BPT classification of Belfiore et al. (2016).

(iv) Mixed galaxies. The fourth row of panels (H, I and J) of Fig. 1 exemplifies the mixed galaxies (NGC 2449, NGC 5971 and IC0540). This class is characterised by star-forming regions (high-ionisation EL regions, where $W_{H\alpha} > 6$ Å),

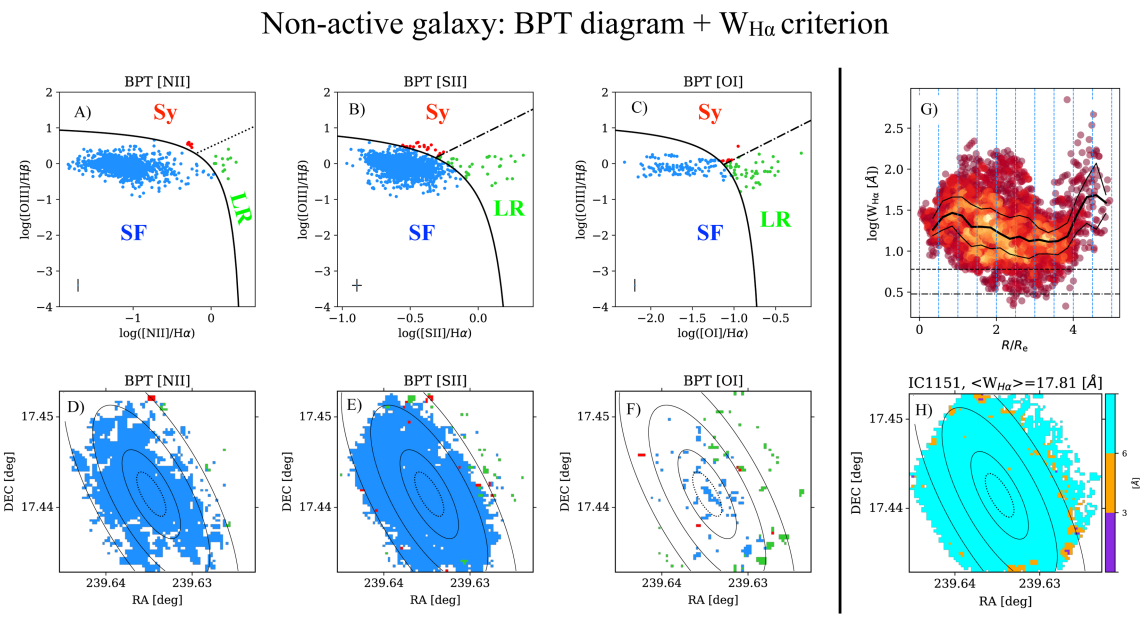

Fig. 2. Galaxy IC1151 as an example of the non-active class based on the BPT diagram and $W_{H\alpha}$ criterion (see Sect. 3). *Panels A, B, and C*: resolved [NII]−,[SII]− and [OI]−BPT diagnostic diagrams, where the solid curve is the empirical star-formation line of Kauffmann et al. (2003) and pixels below this line are dominated by star formation (SF; blue). The division (dash-dotted line) between the Seyfert (Sy; red) and LINER (LR; green) regions in *panels B and C* is adopted from Kewley et al. (2006), while the empirical Seyferts/LINER division (dotted line) in *panel A* comes from Cid Fernandes et al. (2010). *Panels D, E, and F*: resolved [NII]−,[SII]−, and [OI]−BPT maps corresponding to the BPT diagram. *Panels G*: resolved $W_{H\alpha}$ radial profile from individual spaxels, where the dashed-dotted and dashed lines correspond to the thresholds of 3 and 6 Å, respectively. The blue dotted vertical lines define the bins of $0.5R_e$. The black thick line shows the median value of the $W_{H\alpha}$, where the thin black lines indicate the median absolute deviation. *Panel H*: resolved $W_{H\alpha}$ map, where the colour bar indicates the thresholds of the spaxels: $W_{H\alpha} \leq 3$ Å (violet), 3 Å $< W_{H\alpha} \leq 6$ Å (orange) and $W_{H\alpha} > 6$ Å (cyan). The dotted line indicates the region of $0.5R_e$, where the continuous lines mark separation of 1, 2, and $3R_e$. The median value of the $W_{H\alpha}$ for the full maps is given as label in the panel. To classify this galaxy as non-active, the central pixels that are below $0.5R_e$ should not populate the Seyfert region of the BPT diagrams (at least two from the three BPT diagrams), but their $W_{H\alpha}$ values can vary, depending on the quenching stage of the galaxy.

intermediate-ionisation EL regions (3 Å $< W_{H\alpha} \leq 6$ Å), and low-ionisation emission-line regions ($W_{H\alpha} \leq 3$ Å) with no clear morphological pattern on the $W_{H\alpha}$ map. The median value of $W_{H\alpha}$ of the galaxy is usually between 3 and 6 Å. A low-ionisation EL region in the centre of the galaxies is possible, but it should be more extended than $0.5R_e$ (to be distinguishable from the centrally quiescent class) or randomly distributed within the disc. This mixed class can be represented by both active and non-active galaxies.

(v) Nearly retired galaxies. The fifth row of panels (K, L and M) of Fig. 1 exemplifies the nearly retired class galaxies (UGC10905, NGC 2554 and NGC 6081), where the median value of the $W_{H\alpha}$ map is equal to or below 3 Å. Similar to the mixed class, nearly retired galaxies have no clear pattern, but these galaxies are mostly dominated by low-ionisation EL regions (i.e. above 90% of the spaxels usually have $W_{H\alpha}$ values equal to or below 3 Å) and little star-formation within $2R_e$ of the galaxy (usually less than 3% of the spaxels have $W_{H\alpha} > 6$ Å). This class cannot be mistaken with the centrally quiescent class in cases where there are low-ionisation ELs in the central regions because members of this class do not have a well-defined star-forming disc beyond $0.5R_e$ as in the centrally quiescent class. The nearly retired class can be represented by both active and non-active galaxies.

(vi) Fully retired galaxies. Panel N of Fig. 1 represents the fully retired class of galaxies (NGC 5485), where the median value of $W_{H\alpha} \leq 3$ Å. The galaxy is fully dominated by these low-ionisation EL regions within 2 R_e of the galaxy. Similar to the centrally quiescent class, the fully retired class is entirely made up of non-active galaxies because the $W_{H\alpha}$ value of the central pixels is always equal to or below 3 Å even in cases where the line ratios populate the Seyfert region of the BPT diagrams. This class is somewhat similar to the eLIER galaxies in the [SII]-BPT classification of Belfiore et al. (2016).

3.2. Nuclear activity criteria

From the BPT diagrams in panels A−C of Figs. 2–4, we define whether the galaxy is active or non-active for each QS (i.e. this is the second dimension of the EL classification QuestNA). If the line ratios of the central spaxels that are below $0.5R_e$ populate the Seyfert region of the BPT diagrams (at least two from the three BPT diagrams), then the galaxy is defined as an AGN-host candidate (three is the minimum number of central pixels that define the nuclear activity of the galaxies based on the point spread function of CALIFA maps).

If the central pixels ($<0.5R_e$) have values of $W_{H\alpha}$ above 3 Å, the nuclear activity classification is reliable, and the galaxy is considered active; otherwise it is labelled non-active (galaxy is also classified as non-active if the line ratios do not populate the Seyfert regions). Once the galaxy is classified as active, we further define whether it hosts a weak AGN, where the $W_{H\alpha}$ values of the central pixels range between 3 and 6 Å, or a strong AGN, where the $W_{H\alpha}$ values of the central pixels go above 6 Å. The corresponding resolved maps of the BPT diagrams in panels D−F help us to locate the Seyfert spaxels, and decide whether or not they belong to the centre of the galaxy. Panel G and H show the resolved radial profile and the map of $W_{H\alpha}$, respectively,

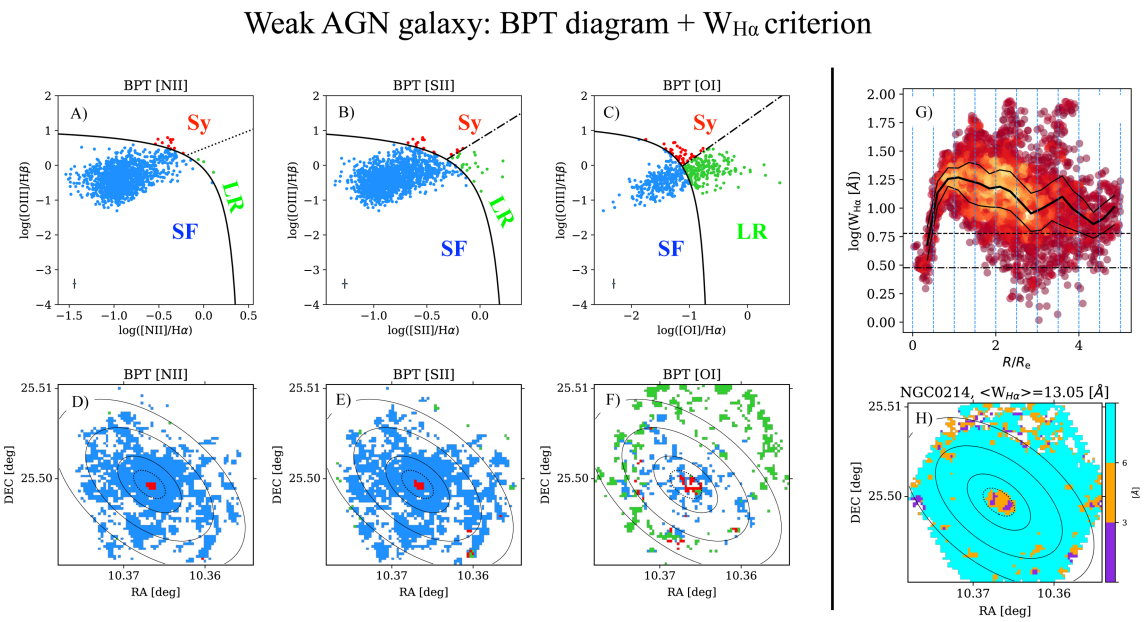

Fig. 3. Galaxy NGC 0214 as an example of a weak AGN class based on the BPT diagram and $W_{H\alpha}$ criterion (see Sect. 3). Description as per Fig. 2. To classify this galaxy as wAGN, the central pixels that are below $0.5R_e$ should have values 3 Å $< W_{H\alpha} \leq$ 6 Å, and they should populate the Seyfert (Sy) region of the BPT diagrams (at least two from the three BPTs).

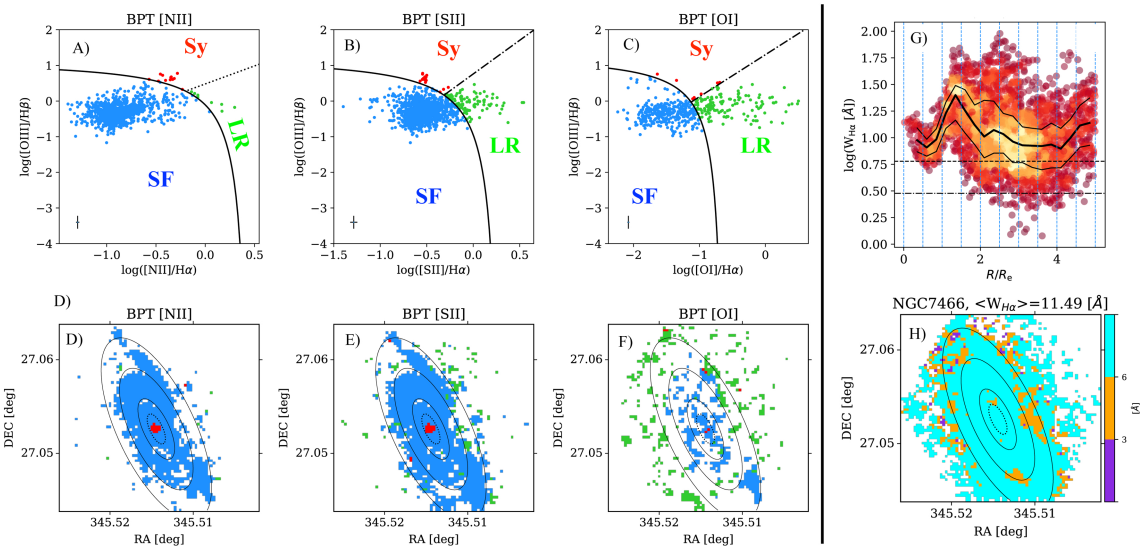

Fig. 4. Galaxy NGC 7566 as an example of a strong AGN class based on the BPT diagram and $W_{H\alpha}$ criterion (see Sect. 3). Description as per Fig. 2. To classify this galaxy as sAGN, the central pixels that are below $0.5R_e$ should have $W_{H\alpha}$ values above 6 Å and they should also populate the Seyfert (Sy) region of the BPT diagrams (at least two from the three BPTs).

which are needed for applying the thresholds of the nuclear activity classification (i.e. 3 and 6 Å of the $W_{H\alpha}$). All resolved maps and BPT diagrams for the rest of the sample are shown in Appendix A.

3.3. Uncertainties on the EL classification

Using the scheme, we perform a by-eye classification of our galaxy sample, finding 96 star-forming, 12 quiescent-nuclear-ring, 23 centrally quiescent, 37 mixed, 34 nearly retired, and 36 fully retired galaxies (from which 215 non-active, 8 wAGN, and 15 sAGN). Despite the detailed analysis, there are marginal cases in our classification where a galaxy could be slightly below or above certain thresholds of the median $W_{H\alpha}$ and/or its radial profile. Therefore, we attribute a quality index to our classified galaxies: a flag value of 1 indicates an unambiguous QS classification; flag=2 indicates uncertain QS classification due to complex $W_{H\alpha}$ morphology; and flag=3 indicates uncertain QS classification due to bad data. Approximately 10% of the galaxies have uncertain QS classification (flag=2 or 3). On the other hand, the quality index, related to the nuclear activity classification includes sure (S) and unsure (U) cases, depending on whether the nuclear activity is confirmed by three or two of the BPT diagrams, respectively (nine galaxies have label=U, which is ~4% of the total of 238 galaxies

and ∼40% of the total active galaxies). The QS and NA classification labels, with the corresponding flags for all 238 CALIFA galaxies, are given in Table B.1.

For the AGN (weak and strong) classes, it is possible that the ionisation in the centre of the galaxy, shown in the Seyfert region of the BPT diagrams, is caused by star-formation-driven shocks rather than the AGN itself (e.g. López-Cobá et al. 2019). In this case, the galaxies typically show a bi-conical outflow from the centre of the galaxy to the outskirts, confirmed by the velocity-to-velocity dispersion ratio of the galaxy in the central regions. López-Cobá et al. (2019) examined 667 CALIFA galaxies from DR3 (Sánchez et al. 2016a) in which our sample is included and defined 17 galaxies with star-formation-driven outflows. We compare our sample with theirs, and we only exclude the galaxy NGC 0681 from our list of the wAGN candidates due to the presence of outflow.

We also compare our AGN results with the list of bona fide AGN host galaxies, defined by Lacerda et al. (2020) from the extended sample of CALIFA survey (Sánchez et al. 2016a, Galbany et al. 2018). There is an overlap of 10 galaxies (eight galaxies in the sAGN class: UGC03995, MCG-02-02-030, UGC00987, NGC 2410, IC2247, NGC 2639, IC0540, NGC 3160 and two galaxies in the wAGN class: NGC 2554 and NGC 6762) from the total 23 AGN (15 sAGN and 8 wAGN) host galaxies in our sample. We classify more galaxies as having AGN because of the more relaxed criteria we adopt in our study compared to Lacerda et al. (2020). Specifically, we require the Seyfert region of the BPT diagrams to be populated at least for two of the three diagrams but Lacerda et al. (2020) require population in all three diagrams. The goals of these two studies are different: Lacerda et al. (2020) focus on the bona fide cases of AGN hosts and exclude some boarder cases, while we aim to record any possibility of AGN activity in the galaxy. For example, NGC 1167, which has a strong AGN in the centre (e.g. Struve et al. 2010), is included in our AGN sample but would be excluded by the stricter requirements of Lacerda et al. (2020). Outflows and shocks are not included in the current 2D EL classification since it is out of the scope of the current study. On the other hand, it might be possible to add their categorisation to the nuclear activity criteria and expand the EL classes.

Finally, we might expect to find more EL classes or subclasses with improved spectral and spatial resolution data, and a higher number of sample statistics in comparison to the current sample (e.g. the AMUSING ++ survey, López-Cobá et al. 2020).

4. Characteristic $W_{H\alpha}$ radial profiles of the EL galaxies

To classify the galaxies in their corresponding EL classes, we use set of figures and diagrams for each galaxy as discussed in Sect. 3. One important element is the $W_{H\alpha}$ radial profile, which provides a detailed information about the distribution of the retired and the star-forming regions of the galaxies.

In Fig. 5, we show the characteristic (stacked) $W_{H\alpha}$ radial profiles of all galaxies in each EL class. The profiles are obtained through a radial map positioned in the centre of the galaxy and projected on the plane of the galaxy, assuming the position angle and inclination reported in Table B.1 of K17. Similarly to Fig. 1, the rows of Fig. 5 correspond to the QSs of the galaxies, and the columns correspond to their nuclear activity groups. The nuclear activity leaves a clear trace within roughly $0.2R_e$ of the profiles: $W_{H\alpha} > 3$ Å for wAGNs (middle column), $W_{H\alpha} > 6$ Å for sAGNs (right column), while this value is not fixed for the non-active galaxies (left column).

Further, we compare the median profiles of the galaxy in each QS for the three different nuclear activity groups in Fig. 6. The details of those profiles vary significantly between the classes (especially within $0.5R_e$), but the average value of $W_{H\alpha}$ generally increases from the centre of the galaxy to the outskirts. This might indicate that the star formation quenching in the galaxies largely proceeds 'inside-out', which has been noticed for CALIFA galaxies elsewhere (e.g. González Delgado et al. 2016; Belfiore et al. 2017; Lin et al. 2017; Ellison et al. 2018; Sánchez et al. 2018). Nevertheless, patterns can be more complicated as shown by the mixed and retired classes.

The star-forming galaxy group shows the highest radial values of $W_{H\alpha}$, well above the 6 Å threshold (see also panels A, B, and C in Fig. 5), where the radial median of $W_{H\alpha}$ is larger than 13 Å at each radii). This is particularly clear for the non-active group in the left panel of Fig. 6, which contains the largest statistical sample of galaxies.

Considering the nuclear activity in particular, the median profile of the sAGN galaxies is between 3 and 6 Å, which is below that of the non-active galaxies across the radial extent of the profile. The wAGN profile is roughly similar to the non-active profile for the star-forming QS, except within $0.5R_e$ where they differ by ∼10 Å. Nevertheless, for the other QSs the difference between the profiles from the three nuclear activity groups is less evident.

Similarly high values ($W_{H\alpha} \sim 10$ Å) are reached by the median radial profiles of quiescent-nuclear-ring and centrally quiescent classes beyond one effective radius. Within $1R_e$, instead, both profiles show a dip below $W_{H\alpha} = 3$ Å that characterises quenched regions (see also panels D and G in Fig. 5). Nevertheless, the central radial bin (where $R = 0.25R_e$) of the quiescent-nuclear-ring class shows values that are again above the threshold that defined star formation dominance (6 Å).

It is interesting to note the case of the mixed profile, which is constantly in the range $3 \text{ Å} < W_{H\alpha} \leq 6$ Å, except in the central bins where the radial median of $W_{H\alpha}$ is below 3 Å (see also panel F of Fig. 5). This might be an indication that for this class, which generally presents a complex star formation pattern, the quenching begins from the very centre. Further, in Fig. 6, the mixed−wAGN profile in the regions of $R > 2R_e$ goes above the $W_{H\alpha} = 6$ Å demarcation line (see also Fig. 5, panel I). This profile is generated by a single galaxy and may not be representative of the mixed-wAGN category.

Nearly retired and fully retired galaxy groups show $W_{H\alpha}$ almost constantly below the 3 Å threshold that marks ionisation by post-AGB star dominance. Both profiles increase in values from the centre to the outskirts, but the nearly retired profile is always above the fully retired median profile. In addition, the nearly retired galaxy group profile reaches values of $W_{H\alpha} > 3$ Å, where $R > 3R_e$, which might indicate some weak star formation activity in this region. The profiles from the AGN-host galaxies in the nearly retired stage are approximately equivalent to their non-active counterparts.

5. Global properties of the galaxies at different quenching stages

To understand the typical properties of each EL class, we investigate some basic parameters of the studied stellar systems. The results show that the EL classes are characterised by specific

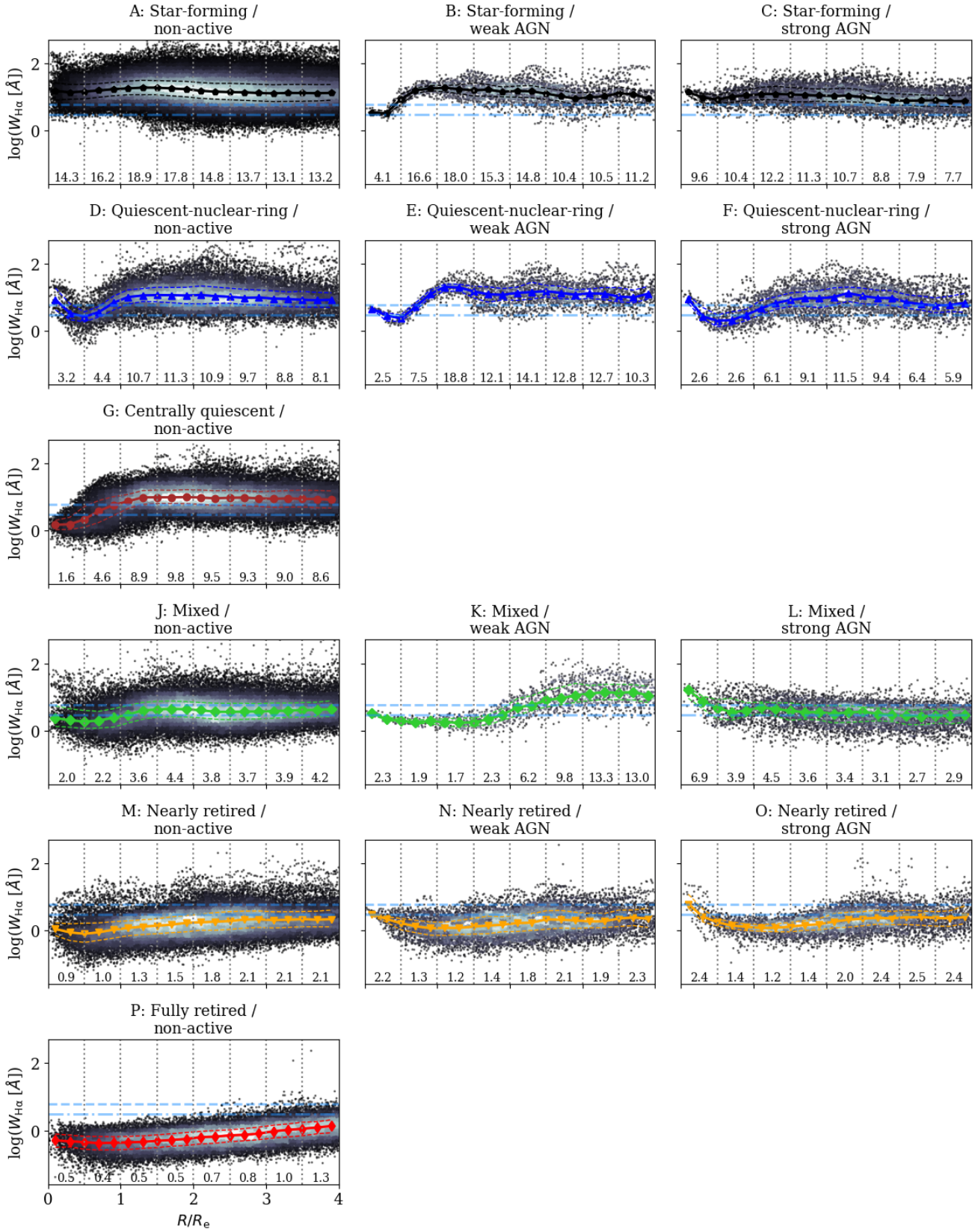

Fig. 5. Stacked radial profiles versus equivalent width of Hα ($W_{\mathrm{H}\alpha}$) for the galaxies in the different emission-line classes, normalised by galaxy effective radius R_{e} (Sect. 4). The coloured full lines show the median of the radial distributions, and the coloured dashed lines indicate the 25th and 75th percentiles of the radial distributions. The blue dash-dotted and dashed horizontal lines display constant $W_{\mathrm{H}\alpha}$ = 3 Å and $W_{\mathrm{H}\alpha}$ = 6 Å values, respectively. The numbers at the bottom of each panel show the median $W_{\mathrm{H}\alpha}$ in a given radial bin of $0.5R/R_{\mathrm{e}}$. Bins are separated by vertical, black, dashed lines.

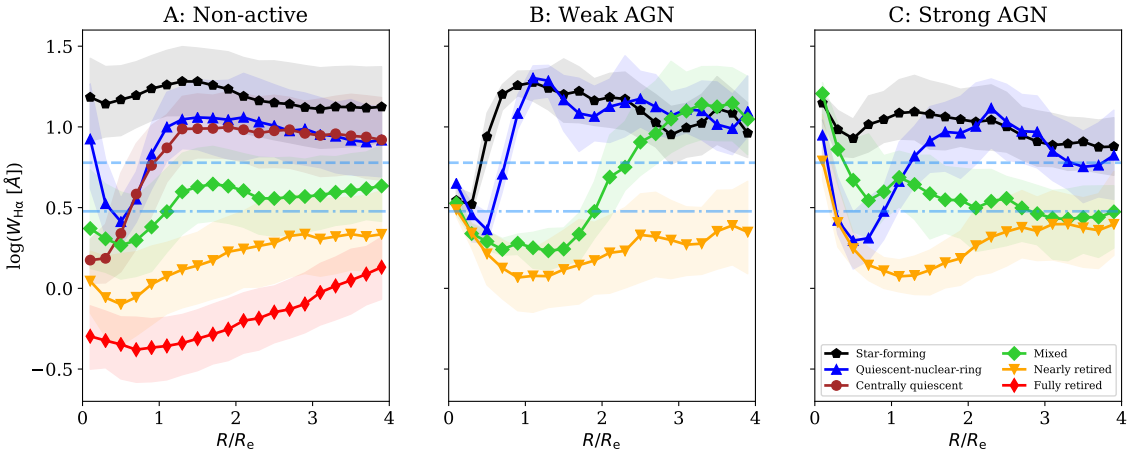

Fig. 6. Median radial profiles equivalent width of Hα ($W_{H\alpha}$) for our sample of galaxies in each quenching stage for non-active (*left*), weak AGN (*middle*), and strong AGN (*right*) classes, normalised by galaxy effective radius R_e (Sect. 4). The shaded regions express the 25th and 75th percentiles of the radial distributions. The blue dash-dotted and dashed horizontal lines display $W_{H\alpha}$ = 3 Å and $W_{H\alpha}$ = 6 Å thresholds, respectively. The variation in the $W_{H\alpha}$ profile suggests an 'inside-out' star-formation quenching scenario for our sample of galaxies.

properties of the galaxies, indicating that QuestNA is a valid classification method.

5.1. Morphology

The morphology of similar emission-line class galaxies has been broadly explored in the literature (e.g. Schawinski et al. 2007; Sánchez et al. 2018, 2019; Lacerda et al. 2020), and is an important parameter that gives direct information about the structural characteristics of the galaxies in the various categories. In Fig. 7, we show the distributions of our EL classes through the Hubble sequence using the CALIFA classification of Walcher et al. (2014). In general, the morphology changes from late- to early-type moving from the star-forming to the retired classes.

Examining the non-active galaxies (continuous lines is Fig. 7), the star-forming class are mainly late-type spirals (Sb–Sdm), while quiescent-nuclear-ring and centrally quiescent systems are represented by early-type spirals (Sab–Sbc). Similarly to the centrally quiescent and quiescent-nuclear-ring objects, the mixed class possesses early-type spiral morphologies (Sa–Sb), but it also includes a few cases of lenticulars (S0–S0a) and ellipticals (E4–E7). Furthermore, the nearly retired and fully retired classes of the non-active galaxies are mainly presented by lenticular and elliptical galaxies.

In total, the sAGN class (slashes in Fig. 7) is mostly represented by early-type spiral (Sa–Sbc) and lenticular (S0–S0a) galaxies. Similarly, the wAGN class (circles in Fig. 7) spans over the early-type spiral (Sa–Sbc) and lenticular (S0-S0a) systems, but also includes older galaxies such as the ellipticals (E4–E7). The comparison between the distributions of the active and non-active galaxies shows a mismatch for the star-forming and nearly retired QSs. Panel B of Fig. 7 of the star-forming QS shows that the sAGNs are represented by early-type spiral galaxies (Sa–Sbc), which differs from the main peak of the non-active galaxies' distribution, located towards the late-type spirals. Furthermore, panel F of Fig. 7 of the nearly retired QS indicates that the wAGNs span over the early-type galaxies and early-type spirals, where the latter is an outlier region for the distribution of non-active galaxies, peaking at the lenticular galaxies.

We also make a structural comparison between the active and non-active group, taking into account the presence of a sure (B) or unsure (AB) bar in each quenching group based on CALIFA bar classification of Walcher et al. (2014). Figure 8 shows that the highest number of barred galaxies belong to the quiescent-nuclear-ring QS, followed by the centrally quiescent and mixed groups. The upper error-bar of the histograms represents the maximal number of bars in a group, which includes both bars (B) and unsure bar (AB) cases of the galaxies (see also Table B.1). The information from the morphological and bar classifications of Walcher et al. (2014) for our sample suggest that the secular evolutionary processes (which involve the internal evolutionary phenomena induced by dynamical features such as spiral arms and bars) are much more prominent in the quiescent-nuclear-ring, centrally quiescent, and mixed classes than in the remaining classes.

5.2. Photometric, stellar, kinematic, and dynamical properties

Besides the galaxy morphology, our classification correlates with a large set of galactic properties as shown in Fig. 9. This proves that knowledge of the QS of a galaxy is sufficient to access the average value of a variety of parameters. The bulge-to-disc ratios (B/D, panel A); the stellar mass surface density (μ_*, panel D); the stellar age (τ, panel F); the stellar metallicity (Z, panel G); and the peak circular velocity ($V_{c,max}$, panel J) all increase moving from the star-forming to the fully retired groups for the non-active galaxies. Conversely, the SFR sharply decreases across the QSs (panel H).

For other properties, the trends are less obvious. Regarding the total luminosity (L_r^{tot}, panel B), the brightest galaxies, on average, are observed within the nearly retired class, and not within the fully retired ones, while galaxies in the star-forming class are the faintest objects. A similar trend is shown by total stellar and dynamical mass (M_*, panel E; and M_{dyn}^{tot}, panel K; respectively), while the opposite behaviour is observed for angular momentum (λ_{R_e}, panel I). The size of the galaxies inferred from the median effective radius, R_e, shows a complicated behaviour across the stages (panel C). The largest-size galaxies are mainly quiescent-nuclear-ring galaxies ($R_e \sim 5.35$ kpc) and nearly retired ($R_e \sim 4.89$ kpc), followed by the centrally quiescent ($R_e \sim 4.81$ kpc). Fully retired galaxies have the smallest $R_e \sim 2.23$ kpc in comparison to the rest of the classes, which might indicate that most of the luminosity is generated by their large spheroidal components (considering their large B/D ratio).

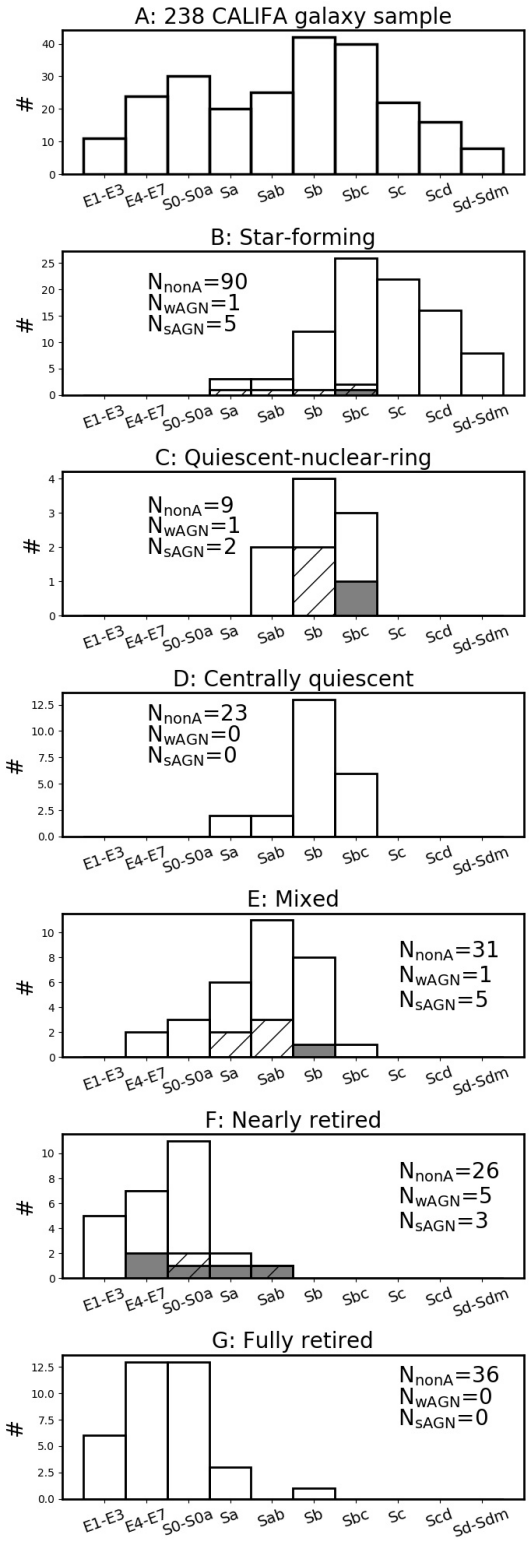

Fig. 7. Distributions of the active and non-active galaxies in each quenching stage through Hubble type (*panels B-G*). The blank bars outline the distribution of the non-active galaxies, while the grey-filled bars and the slashes correspond to the wAGN and sAGN distributions, respectively. *Panel A*: distribution of the full sample. *N* gives the number of the galaxies for each nuclear activity group (see Sect. 5.1).

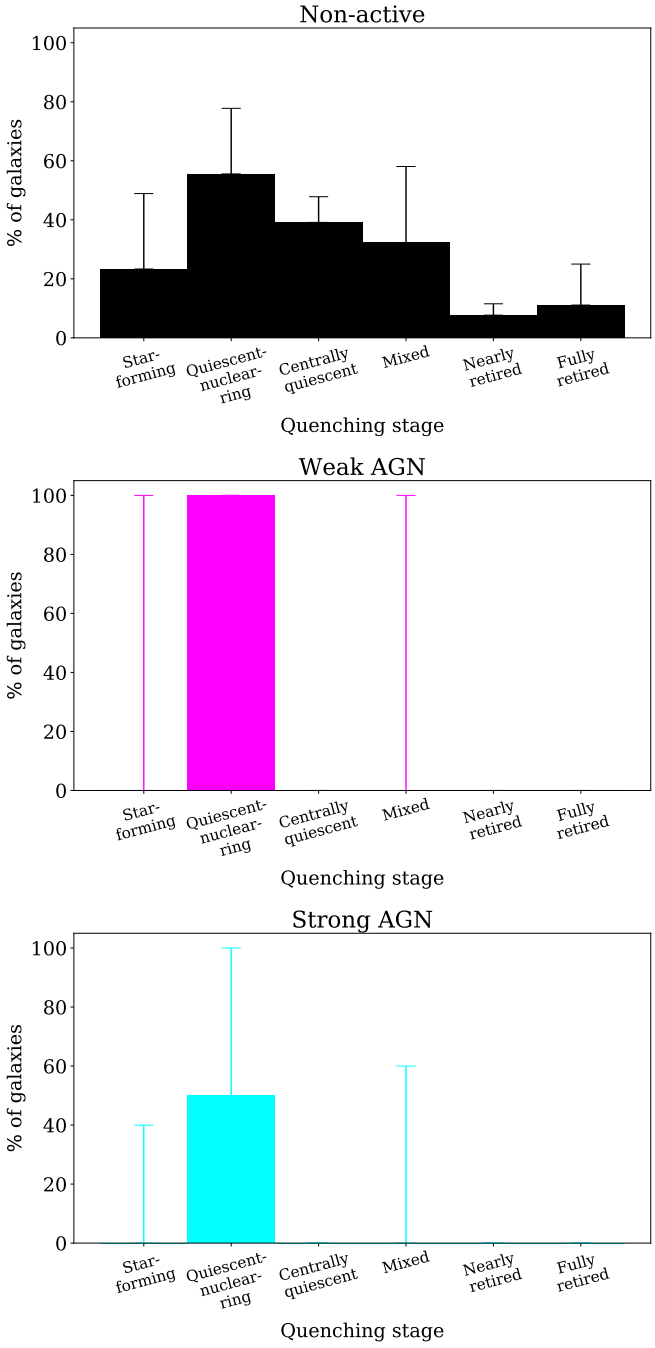

Fig. 8. Distributions of the barred galaxies through active and non-active galaxies for each quenching stage of our sample. The upper error-bar for each stage indicates the fraction of galaxies with the unsure bar. Quiescent-nuclear-ring is represented by the highest number of barred galaxies, followed by centrally quiescent and mixed groups (see Sect. 5.1).

The mass discrepancy factor $f_{\rm d} = 1 - (M_*^{\rm tot}/M_{\rm dyn}^{\rm tot})$ (panel L) displays a rather flat behaviour. We find that $f_{\rm d}$ is largest for star-forming galaxies ($f_{\rm d} = 80\%$) in comparison to the rest of the quenching classes, where $f_{\rm d}$ varies between 64 and 68%. The large value of $f_{\rm d}$ through EL classes could be due to the non-universal nature of the galaxy IMF (e.g. Hoversten & Glazebrook 2008; Cappellari et al. 2012; Lyubenova et al. 2016), radial variation of stellar mass-to-light ratio γ_* (e.g. García-Benito et al. 2019), or the presence of dark matter mass (e.g. Das et al. 2020). The variation of the mass discrepancy could also be explained with an uncounted gas mass in the galaxies, and this is expected to be significant for late-type systems (e.g. McGaugh et al. 2000). In forthcoming papers, we will infer the total gas

mass fractions of our sample using a dust-to-gas calibration (see Barrera-Ballesteros et al. 2018) or CO data (from Bolatto et al. 2017; Colombo et al. 2020) and HI data (Kalinova et al., in prep.) to calculate the dark matter content for each galaxy. The median values of the galaxy properties from the box-and-whisker diagrams are listed in Table B.2.

The behaviour of the AGN-host galaxies at a given QS is also reported in Fig. 9. The sAGN galaxies within the star-forming class are the objects that show the most discrepant behaviour with respect to their non-active counterparts. Those galaxies are mostly located in the upper end of the distributions of all parameters, except for the SFR (panel H), where sAGN galaxies show global SFRs similar to the non-active objects in the same class. However, star-forming-sAGN appear between the objects of the star-forming class with the lowest $f_{\rm d}$. AGN-host galaxies that belong to the mixed and nearly retired categories seem to show low values of $R_{\rm e}$.

6. Discussion

6.1. Imprints of galaxy evolution in the EL classes

To understand whether our proposed categories are linked to galaxy evolution, we superimpose the EL classes on the SFR-M_* diagram (Fig. 10). Galaxies in the star-forming class almost fully populate the SFMS (Fig. 10, panel B). However, the AGN-host galaxies at this QS mostly show strong AGN activity and are located at the upper end of the SFMS, occupied by high-mass galaxies. Quiescent-nuclear-ring and centrally quiescent galaxies appear to populate the green valley of star formation, which is generated by objects that are switching off their star formation in the central region (Fig. 10, panel C and D, respectively). Galaxies with an undefined distribution of the ionisation (mixed class) spread from the SFMS to the red sequence, but they appear mostly located in the green valley as well (Fig. 10, panel E). Strong AGN-host galaxies appear well distributed across the full high-mass region of the SFR-M_* diagram. Nearly retired and fully retired galaxies are tightly constrained along the red sequence. In particular, nearly and fully retired galaxies dominate the high-mass and low-mass ends of the red sequence, respectively. It is interesting to note that the nearly retired galaxies are the most massive systems from our sample, which are also the most dispersion-dominated galaxies (i.e. they have the lowest $\lambda_{R_{\rm e}}$, panel I of Fig. 9) with the largest size stellar discs among the other classes (panels A and C of Fig. 9). These latter are old stellar population galaxies, but still have a little star-formation activity within the $2R_{\rm e}$. This suggests that maybe the fully retired class are the progenitor of the nearly retired class, where star formation has been reignited in the galaxies by merger events or environmental processes in earlier epochs, or that the two classes might have followed independent evolutionary paths since the beginning of their formation (or a combination of both mechanisms). To understand more about the origin of the nearly- and fully retired galaxies, in our next article we will link the QS of the galaxies and their dynamical properties (Kalinova et al., in prep.).

Further, AGN galaxies at the nearly retired stage appear to be mostly in the 'weak' category. This might indicate that the AGN activity reduces with the evolution of the galaxies and the progression of the quenching, possibly due to the progressive diminution of the gas supply.

Panels B and C collect the position of all wAGN and sAGN galaxies independently of their quenching stage. The location of the AGN host galaxies in the transition region between the blue cloud and the red sequence has been reported in other works (e.g. Schawinski et al. 2014; Sánchez et al. 2018; Cano-Díaz et al. 2019; Lacerda et al. 2020). The wAGN galaxies are largely dispersed between the green valley and the red sequence, and mostly occupy either the low-mass or high-mass end of the SFR-M_* diagram. Further, they also show bi-modality in their properties (see also Heckman & Best 2014).

A quicker way to investigate the properties of the galaxies in respect to their position on the SFR-M_* diagram and connect to their stage of evolution (e.g. Ellison et al. 2018; Thorp et al. 2019; Bluck et al. 2020) is provided by Fig. 11, which summarises the distribution of Δ SFR, where $\Delta\mathrm{SFR} \equiv \log \mathrm{SFR} - \log \mathrm{SFMS}$. Here, Δ SFR is the logarithmic distance from the SFMS of Elbaz et al. (2007) using the method described in Bluck et al. (2016). In the figure, the normalised histogram represents local galaxies from SDSS DR7 with a given Δ SFR. In general, the SDSS histogram in grey highlights the fact that galaxies at $z \sim 0$ are mostly located in the red sequence, followed by the blue cloud, and the green valley. In the figure, the QSs of non-active galaxies are indicated with the median and the median absolute deviation of Δ SFR of the given subsamples. Quenching-stage galaxies appear well divided through Δ SFR, indicating how a given QS represents a relatively narrow range of certain physical parameters, validating our classification as a useful tool to trace galaxy evolution through the star formation and nuclear activity. Only the median absolute deviation bars of mixed and centrally quiescent classes overlap in the green valley region.

Furthermore, in Fig. 11 for a given QS, we explore how the ΔSFR values of the active galaxies (grey star for sAGN and grey square for wAGN) are comparable with the ΔSFR median value (coloured symbols) and median absolute deviation (colour bars) of the non-active systems. Overall, star-forming sAGN galaxies show the biggest mismatch with the distribution of their non-active counterparts; they are all shifted towards lower ΔSFR values (i.e. they all deviate from the SFMS) than the star-forming non-active objects. This suggests that the suppression of the star-formation has already started in these galaxies and might be related to the presence of the AGN in their centres through feedback processes (e.g. Frigo et al. 2019; Kauffmann & Haehnelt 2000).

6.2. Inside-out quenching and the role of AGNs

Through our EL classification, we observe that the galaxies on their way to quenching always begin to switch off their star formation from the centre (see Fig. 6). The quiescent-nuclear-ring galaxies are an exception (because they have some instance of star formation below $0.2R_{\rm e}$) but also a rare example, and they are mostly quenched within $0.3{-}0.5R_{\rm e}$. In other words, we rarely observe a galaxy that is largely star forming in the centre and fully quenched in the outskirts. Usually, this is due to the presence of a close companion or interaction between galaxies (which have been purposely excluded from the sample analysed here). Outside-in star-formation quenching may also be induced by ram-pressure stripping in galaxy cluster environments (e.g. Bekki 2009; Vulcani et al. 2020).

Our results are consistent with an 'inside-out' quenching scenario (e.g. González Delgado et al. 2016; Catalán-Torrecilla et al. 2017; Belfiore et al. 2018; Sánchez et al. 2018; Lin et al. 2019; Lacerda et al. 2020), which predicts that the star-formation quenching starts from the centre of the galaxies due to the presence and the continuous growth of the bulge (e.g. Martig et al. 2009). Galaxies with a larger central mass concentration are expected to host more massive black holes (BHs) from the $M_{\rm bulge} - M_{BH}$ relation (e.g. Marconi & Hunt 2003; Häring & Rix 2004; McConnell & Ma 2013), and experience more significant energetic feedback. Thus, the growth of the

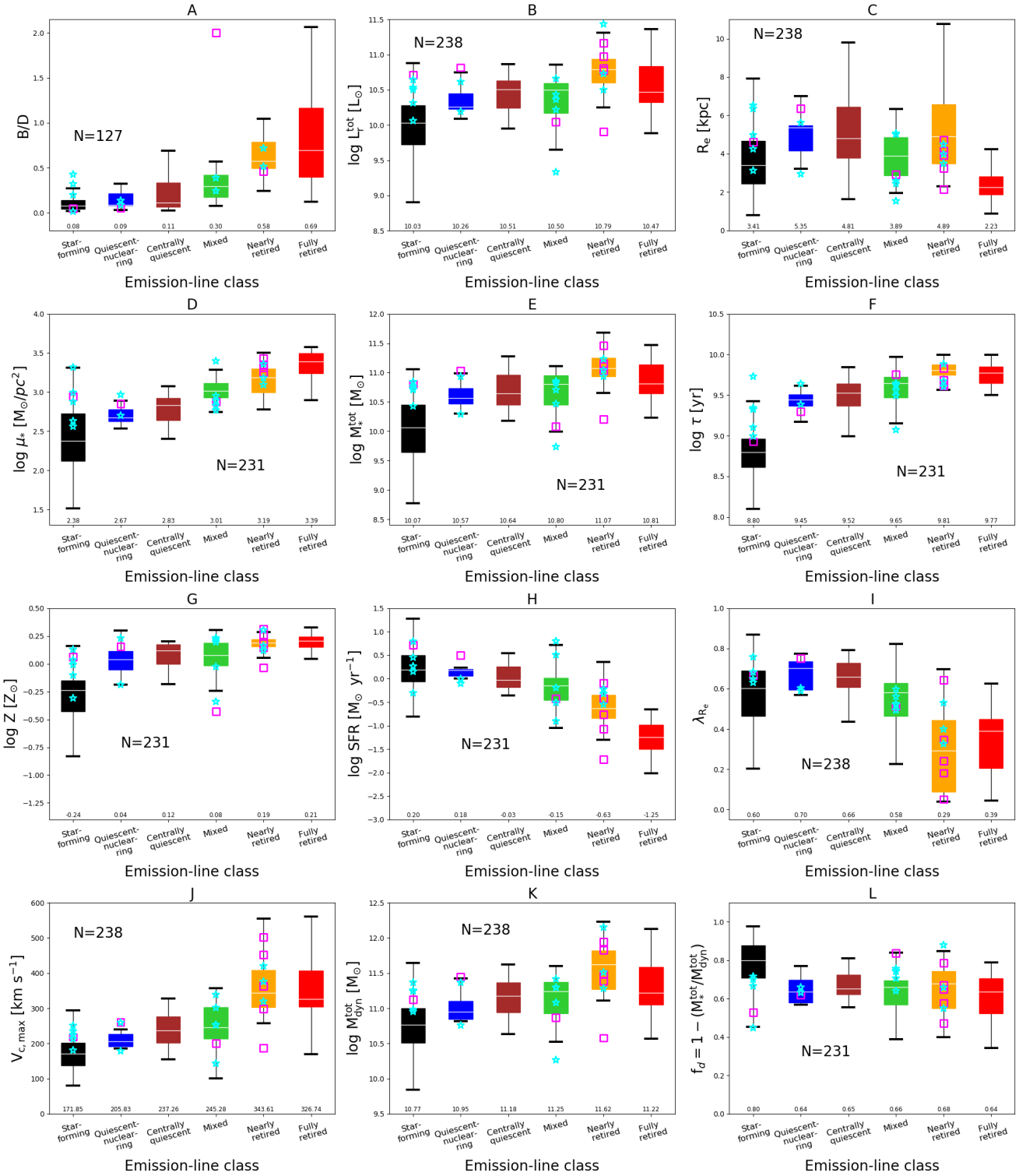

Fig. 9. Box-and-whisker diagrams of basic galaxy properties through the EL classification (see Sect. 5). The colour diagrams represent the properties of the non-active galaxies as follows: black – star-forming; dark blue – quiescent-nuclear-ring; brown – centrally quiescent; green – mixed; orange – nearly retired; and red – fully retired. The active galaxies are over-plotted with empty symbols on the diagrams for a given quenching stage (cyan star for sAGN and magenta square for wAGN). The boxes represent the data between the lower and the upper quartiles of the distribution with median values (Tukey 1977), given by the white lines and the numbers. The extent of the data outside the quartiles (whiskers) is indicated by the vertical black lines. The label '*N*' in each panel gives the total number of the galaxies participating in the statistics. These diagrams represent distributions of various galactic properties in the different emission-line classes: bulge-over-disc flux ratio (B/D, *panel A*); total luminosity in *r*-band (L_r^{tot}, *panel B*); effective radius (R_e, *panel C*); stellar mass surface density (μ_*, *panel D*); stellar mass (M_*, *panel E*); stellar age (τ, *panel F*); stellar metallicity (Z, *panel G*); star formation rate (SFR, *panel H*); specific angular momentum (λ_{R_e}, *panel I*); peak circular velocity ($V_{c,max}$, *panel J*); total dynamical mass (M_{dyn}^{tot}, *panel K*); and mass discrepancy factor (f_d, *panel L*). The SF–sAGN galaxies show the most discrepant behaviour with respect to their non-active counterparts. The median values of the galaxy properties from the box-and-whisker diagrams are given in Table B.2. See text in Sects. 2 and 5 for further details.

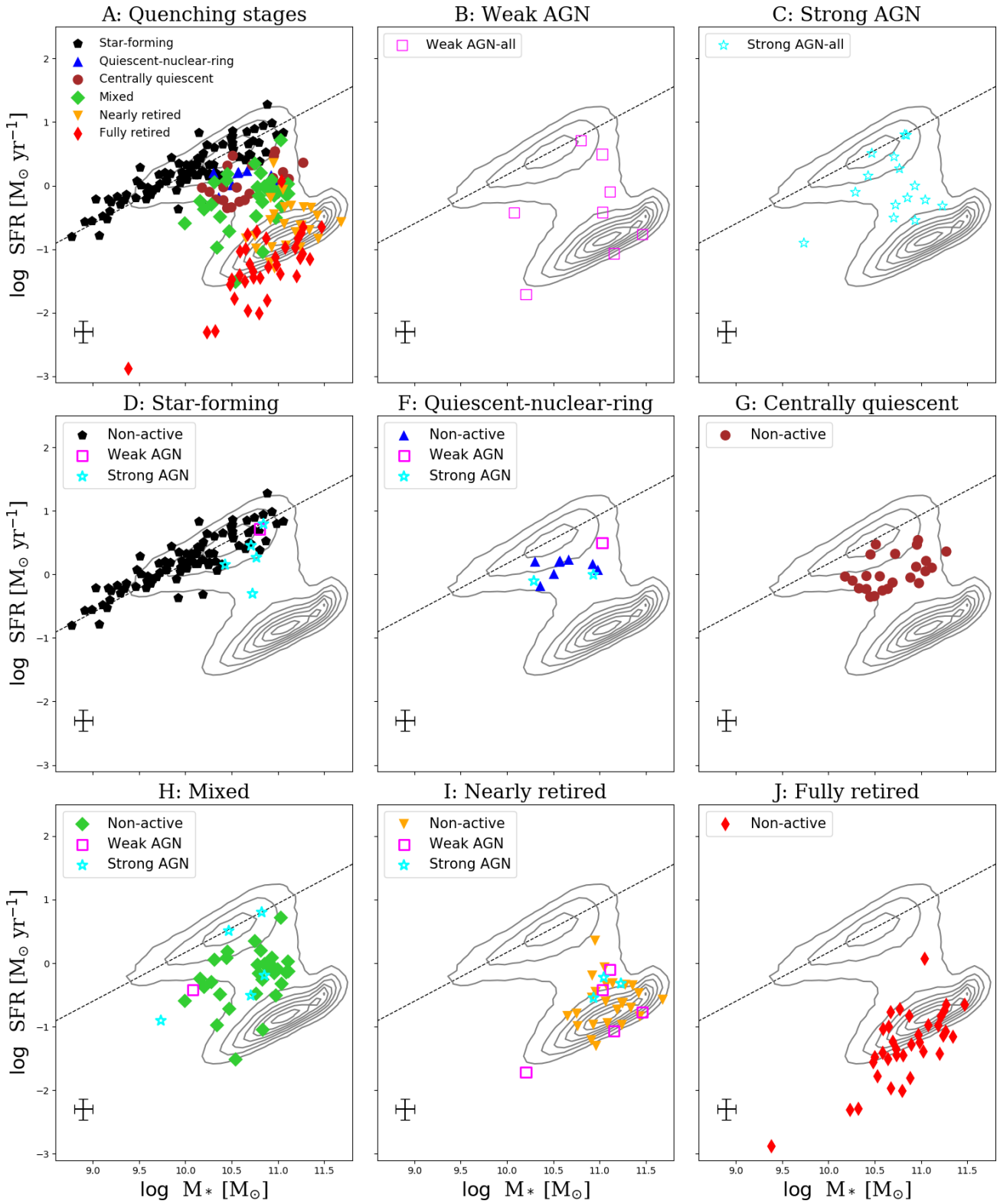

Fig. 10. SFR-M_* for our sample of CALIFA galaxies, considering their quenching stages and nuclear activities (see Sect. 6.1). All active and non-active galaxies through quenching stage are presented in *panel A*. *Panels B and C*: galaxies that host a weak or strong AGN (respectively), independently of their quenching stage. *Panels D–J*: galaxies in a given quenching stage, where the filled symbols represent the non-active galaxies, while the empty symbols correspond to the active galaxies: wAGN (magenta squares) or sAGN (cyan stars). The dashed line indicates the SFMS using the fit of Elbaz et al. (2007). The grey contours represent the SDSS DR7 population for reference from the MPA-JHU catalogue (Kauffmann et al. 2003; Brinchmann et al. 2004; Salim et al. 2007). The error bars in the panels represent the typical uncertainties on the stellar masses and the SFRs, adopted from Cid Fernandes et al. (2014) and González Delgado et al. (2017), respectively. The degree of star-formation quenching increases along the present EL-pattern sequence from star-forming to fully retired. For a given QS, the active galaxies occupy the same domain on the SFR-M_* diagram as the non-active ones.

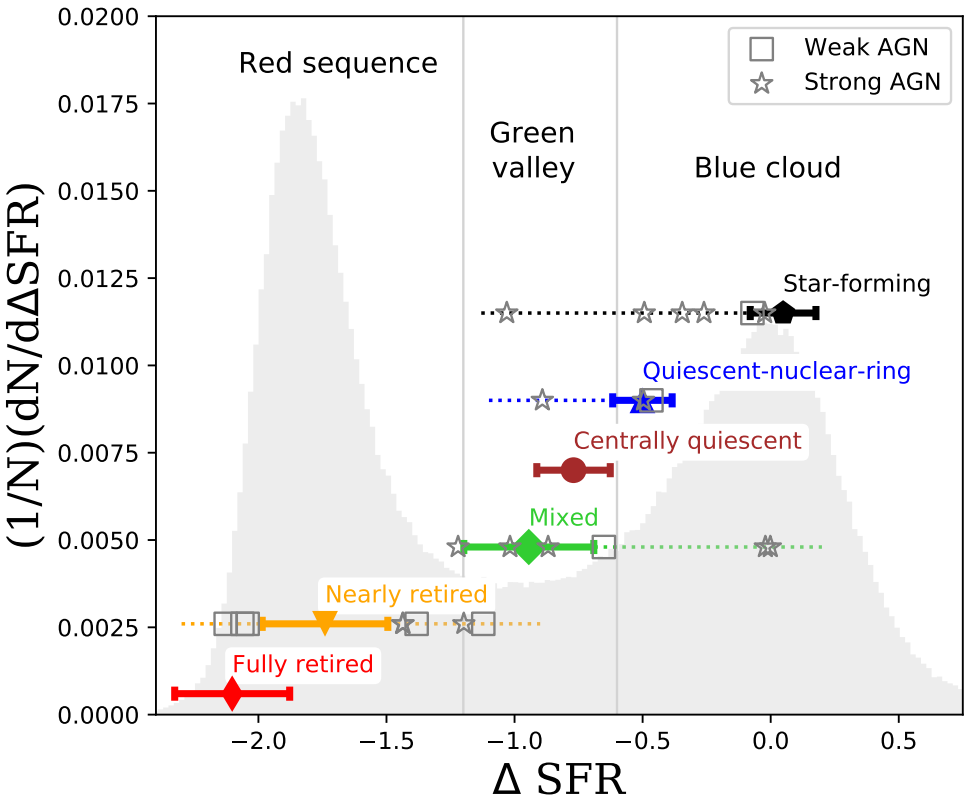

Fig. 11. Distribution of Δ SFR for SDSS DR7 galaxies at $z \sim 0$ (shaded regions; MPA-JHU catalogue, Kauffmann et al. 2003; Brinchmann et al. 2004; Salim et al. 2007) and for our sample of galaxies. The SDSS y-axis gives the number of the galaxies per given ΔSFR bin (i.e. dN/dΔSFR), normalised to the total number N of the SDSS galaxies, while the y-axis of our sample is arbitrary and chosen here only for representative purposes (due to the smaller number of our galaxies in contrast to the number of the SDSS galaxies). The vertical grey lines indicate the green valley region (adopted values from Bluck et al. 2016). The colour symbols indicate the median Δ SFR distribution for the non-active galaxies of our sample in each QS, while the colour bar indicates the corresponding median absolute deviation. The active galaxies are represented by the grey empty symbols (stars for sAGNs and squares for wAGNs). The horizontal dotted colour lines are plotted to guide the eye for the position of the active galaxies in comparison to the non-active ones for a given QS. Quenching stage galaxies are well divided through Δ SFR, suggesting that the QS represents a certain evolutionary phase from the life cycle of the galaxy (see Sect. 6.1).

central spheroid could explain the precedence of the inside-out over the outside-in quenching scenario for the evolution of our galaxies (e.g. González Delgado et al. 2016; Ellison et al. 2018; Lin et al. 2019; Bluck et al. 2019).

The proposed EL classification is mostly based on the morphological distribution of the value of $W_{H\alpha}$. This approach presents a unique perspective that allows us to define some EL classes as specific QSs. Nevertheless, we also include the BPT diagrams to search for signatures of AGN ionisation in the galaxies. In particular, while sAGNs are exclusively observed in the green valley of our sample (see also Kauffmann et al. 2003; Salim et al. 2007; Sánchez et al. 2018; Lacerda et al. 2020), galaxies hosting wAGNs are spread over the green valley and the red sequence. A similar bi-modality of the AGNs is also noted by Heckman & Best (2014).

The role of the AGN in the quenching of the galaxies is complex and not yet well understood. AGNs can enhance or suppress star formation in galaxies (e.g. Wagner et al. 2016; Husemann & Harrison 2018; Cresci & Maiolino 2018). For instance, gas outflow from the AGN can trigger the formation of new stars in dense cold gas environments (the so-called positive feedback; Silk 2013; Zubovas et al. 2013; Mahoro et al. 2017). On the other hand, the suppression of star formation can happen via heating of the cold gas or its mechanical removal (the so-called negative feedback; Silk & Rees 1998; Nesvadba et al. 2010; McNamara et al. 2016).

The negative feedback is well accepted in models to regulate massive galaxy growth (e.g. Kauffmann & Haehnelt 2000; Schaye et al. 2015). For example, Frigo et al. (2019) investigate the impact of AGN feedback on the formation of massive galaxies through performance of cosmological simulations and find evidence that the AGN feedback plays an essential role in the formation of quiescent, slow-rotating, triaxial and non-discy early-type galaxies.

We find only a small percentage of AGN-host galaxies in our sample. Similar small percentages have been observed elsewhere, and this has been interpreted as evidence that star-formation quenching in the nearby universe cannot be due to AGN action alone (e.g. Saintonge et al. 2012, 2017; Kirkpatrick et al. 2014). Some studies report that AGN feedback acts locally and does not influence the global SFR budget of the galaxy (e.g. Shin et al. 2019). However, these conclusions could be misleading, because the AGN may no longer be luminous when the effect from the AGN becomes observable (as discussed in Harrison 2017).

Surprisingly, the QSs of active and non-active galaxies seem almost identical (except of centrally quiescent and fully retired QSs, which only represent the non-active galaxy group as described in Sect. 3.1). Additionally, the analysis of active and non-active galaxies at the same QS allowed us to observe that there are no significant differences in the properties of objects with different nuclear activity. An exception is observed for

the star-forming QS, where all AGNs (mainly strong AGNs) in this group are hosted by high-mass and older galaxies that are relatively close to the star-formation green valley. It seems that galaxies do not develop an observable AGN until several of their properties have reached some given value (e.g. the so-called golden mass, Dekel et al. 2019). Future exploration of the gas properties of the EL galaxies will shed more light on the relation between the role of the AGN feedback and the star-formation quenching of the galaxies.

7. Summary

We explore the ionised gas properties of 238 (E1−Sdm) CALIFA galaxies through 2D emission-line classification (QuestNA) based on spatially resolved $W_{H\alpha}$ maps and BPT diagrams ([NI], [SII], [OI]). We define six quenching stages: galaxies dominated by recent star-formation; centrally quiescent galaxies; systems possessing quiescent-nuclear-ring-like structure; galaxies with mixed ionised processes; nearly retired galaxies that posses only a few star forming regions, and systems that are completely quiescent (fully retired within $2R_e$). We further divide the galaxies according to their nuclear activity: non-active galaxies, host of a weak (wAGN), or strong AGN (sAGN). The degree of star-formation quenching increases along the present EL-pattern sequence from star-forming to fully retired.

The EL classes occupy certain domains in the SFR-M_* diagram, where star-forming and quiescent-nuclear-ring classes are located within the blue cloud; centrally quiescent and mixed are transient galaxies in the green valley; and nearly and fully retired are members of the red sequence.

The active galaxies do not show significantly different properties from their corresponding non-active counterparts for a given QS, except for the star-forming sAGN class. Overall, the sAGN galaxies are mainly located in the blue cloud or the green valley. On the other hand, the wAGN galaxies are largely dispersed between the green valley and the red sequence, and mostly occupy either the low-mass or high-mass end of the SFR-M_* diagram.

A morphological analysis of our sample indicates that secular evolutionary features (e.g. bar, spiral arms) dominate the structure of quiescent-nuclear-ring, centrally quiescent, and mixed classes in comparison to the other EL classes. The $W_{H\alpha}$ profiles of the EL galaxies indicate an 'inside-out' star-formation quenching scenario and emphasise the importance of the galaxy bulge or central spheroid (see Fig. 6).

In forthcoming papers, we will continue the exploration of the CALIFA galaxies grouped in EL classes through various other properties, such as dynamics, velocity profiles, gas content, and environment, in order to complete the proposed classification and further explore the quenching mechanism of the active and non-active galaxies.

Acknowledgements. We thank the anonymous referee, whose suggestions helped us to improve the quality and presentation of this paper. DC acknowledges support by the Deutsche Forschungsgemeinschaft, DFG project number SFB956A. SFS acknowledge Conacyt projects CB-285080 and FC-2016-01 - 1916, and PAPIIT-DGAPA IN100519. RGB and RGD acknowledges financial support from the State Agency for Research of the Spanish MCIU through the "Center of Excellence Severo Ochoa" award to the Instituto de Astrofísica de Andalucía (SEV-2017-0709), and AYA2016-77846-P. ER acknowledges the support of the Natural Sciences and Engineering Research Council of Canada (NSERC), funding reference number RGPIN-2017-03987. In this study, we made use of the data of the first legacy survey, the Calar Alto Legacy Integral Field Area (CALIFA) survey, based on observations made at the Centro Astronómico Hispano Alemán (CAHA) at Calar Alto, operated jointly by the Max Planck-Institut für Astronomie and the Instituto de Astrofísica de Andalucía (CSIC). This research has made use of the NASA/IPAC Extragalactic Database (NED), which is operated by the Jet Propulsion Laboratory, California Institute of Technology, under contract with the National Aeronautics and Space Administration. Funding for the Sloan Digital Sky Survey IV has been provided by the Alfred P. Sloan Foundation, the US Department of Energy Office of Science, and the Participating Institutions. SDSS-IV acknowledges support and resources from the Center for High-Performance Computing at the University of Utah. The SDSS web site is www.sdss.org. SDSS-IV is managed by the Astrophysical Research Consortium for the Participating Institutions of the SDSS Collaboration including the Brazilian Participation Group, the Carnegie Institution for Science, Carnegie Mellon University, the Chilean Participation Group, the French Participation Group, Harvard-Smithsonian Center for Astrophysics, Instituto de Astrofísica de Canarias, The Johns Hopkins University, Kavli Institute for the Physics and Mathematics of the Universe (IPMU)/University of Tokyo, Lawrence Berkeley National Laboratory, Leibniz Institut für Astrophysik Potsdam (AIP), Max-Planck-Institut für Astronomie (MPIA Heidelberg), Max-Planck-Institut für Astrophysik (MPA Garching), Max-Planck-Institut für Extraterrestrische Physik (MPE), National Astronomical Observatory of China, New Mexico State University, New York University, University of Notre Dame, Observatário Nacional/MCTI, The Ohio State University, Pennsylvania State University, Shanghai Astronomical Observatory, United Kingdom Participation Group, Universidad Nacional Autónoma de México, University of Arizona, University of Colorado Boulder, University of Oxford, University of Portsmouth, University of Utah, University of Virginia, University of Washington, University of Wisconsin, Vanderbilt University, and Yale University. This research made use of Astropy (http://www.astropy.org), a community-developed core Python package for Astronomy (Astropy Collaboration, 2013).

References

Abazajian, K. N., Adelman-McCarthy, J. K., Agüeros, M. A., et al. 2009, ApJS, 182, 543
Alam, S., Albareti, F. D., Allende Prieto, C., et al. 2015, ApJS, 219, 12
Alongi, M., Bertelli, G., Bressan, A., et al. 1993, A&AS, 97, 851
Aquino-Ortíz, E., Valenzuela, O., Sánchez, S. F., et al. 2018, MNRAS, 479, 2133
Baldry, I. K., Glazebrook, K., Brinkmann, J., et al. 2004, ApJ, 600, 681
Baldwin, A., Phillips, M. M., & Terlevich, R. 1981, PASP, 93, 817
Barrera-Ballesteros, J. K., Heckman, T., Sánchez, S. F., et al. 2018, ApJ, 852, 74
Bekki, K. 2009, MNRAS, 399, 2221
Belfiore, F., Maiolino, R., Maraston, C., et al. 2016, MNRAS, 461, 3111
Belfiore, F., Maiolino, R., Tremonti, C., et al. 2017, MNRAS, 469, 151
Belfiore, F., Maiolino, R., Bundy, K., et al. 2018, MNRAS, 477, 3014
Blanton, M. R., & Moustakas, J. 2009, ARA&A, 47, 159
Bluck, A. F. L., Mendel, J. T., Ellison, S. L., et al. 2016, MNRAS, 462, 2559
Bluck, A. F. L., Bottrell, C., Teimoorinia, H., et al. 2019, MNRAS, 485, 666
Bluck, A. F. L., Maiolino, R., Sánchez, S. F., et al. 2020, MNRAS, 492, 96
Bolatto, A. D., Wong, T., Utomo, D., et al. 2017, ApJ, 846, 159
Brammer, G. B., Whitaker, K. E., van Dokkum, P. G., et al. 2009, ApJ, 706, L173
Bressan, A., Fagotto, F., Bertelli, G., & Chiosi, C. 1993, A&AS, 100, 647
Brinchmann, J., Charlot, S., White, S. D. M., et al. 2004, MNRAS, 351, 1151
Bruzual, G., & Charlot, S. 2003, MNRAS, 344, 1000
Bundy, K., Bershady, M. A., Law, D. R., et al. 2015, ApJ, 798, 7
Cano-Díaz, M., Sánchez, S. F., Zibetti, S., et al. 2016, ApJ, 821, L26
Cano-Díaz, M., Ávila-Reese, V., Sánchez, S. F., et al. 2019, MNRAS, 488, 3929
Cappellari, M. 2008, MNRAS, 390, 71
Cappellari, M., & Copin, Y. 2003, MNRAS, 342, 345
Cappellari, M., & Emsellem, E. 2004, PASP, 116, 138
Cappellari, M., Emsellem, E., Krajnović, D., et al. 2011, MNRAS, 413, 813
Cappellari, M., McDermid, R. M., Alatalo, K., et al. 2012, Nature, 484, 485
Catalán-Torrecilla, C., Gil de Paz, A., Castillo-Morales, A., et al. 2015, A&A, 584, A87
Catalán-Torrecilla, C., Gil de Paz, A., Castillo-Morales, A., et al. 2017, ApJ, 848, 87
Chabrier, G. 2003, PASP, 115, 763
Charbonnel, C., Meynet, G., Maeder, A., Schaller, G., & Schaerer, D. 1993, A&AS, 101, 415
Cid Fernandes, R., Mateus, A., Sodré, L., Stasińska, G., & Gomes, J. M. 2005, MNRAS, 358, 363
Cid Fernandes, R., Stasińska, G., Schlickmann, M. S., et al. 2010, MNRAS, 403, 1036
Cid Fernandes, R., Stasińska, G., Mateus, A., & Vale Asari, N. 2011, MNRAS, 413, 1687
Cid Fernandes, R., Pérez, E., García Benito, R., et al. 2013, A&A, 557, A86
Cid Fernandes, R., González Delgado, R. M., García Benito, R., et al. 2014, A&A, 561, A130
Colombo, D., Sanchez, S. F., Bolatto, A. D., et al. 2020, A&A, 644, A97
Cresci, G., & Maiolino, R. 2018, Nat. Astron., 2, 179
Croom, S. M., Lawrence, J. S., Bland-Hawthorn, J., et al. 2012, MNRAS, 421, 872

Das, M., McGaugh, S. S., Ianjamasimanana, R., Schombert, J., & Dwarakanath, K. S. 2020, ApJ, 889, 10
de Amorim, A. L., García-Benito, R., Cid Fernandes, R., et al. 2017, MNRAS, 471, 3727
Dekel, A., Lapiner, S., & Dubois, Y. 2019, ArXiv e-prints [arXiv:1904.08431]
Elbaz, D., Daddi, E., Le Borgne, D., et al. 2007, A&A, 468, 33
Ellison, S. L., Sánchez, S. F., Ibarra-Medel, H., et al. 2018, MNRAS, 474, 2039
Emsellem, E., Monnet, G., & Bacon, R. 1994, A&A, 285, 723
Emsellem, E., Cappellari, M., Krajnović, D., et al. 2007, MNRAS, 379, 401
Espinosa-Ponce, C., Sánchez, S. F., Morisset, C., et al. 2020, MNRAS, 494, 1622
Faber, S. M., Willmer, C. N. A., Wolf, C., et al. 2007, ApJ, 665, 265
Fagotto, F., Bressan, A., Bertelli, G., & Chiosi, C. 1994a, A&AS, 104, 365
Fagotto, F., Bressan, A., Bertelli, G., & Chiosi, C. 1994b, A&AS, 105, 29
Fagotto, F., Bressan, A., Bertelli, G., & Chiosi, C. 1994c, A&AS, 105, 39
Falcón-Barroso, J., Sánchez-Blázquez, P., Vazdekis, A., et al. 2011, A&A, 532, A95
Falcón-Barroso, J., Lyubenova, M., van de Ven, G., et al. 2017, A&A, 597, A48
Falcón-Barroso, J., van de Ven, G., Lyubenova, M., et al. 2019, A&A, 632, A59
Flores-Fajardo, N., Morisset, C., Stasińska, G., & Binette, L. 2011, MNRAS, 415, 2182
Foreman-Mackey, D., Hogg, D. W., Lang, D., & Goodman, J. 2013, PASP, 125, 306
Frigo, M., Naab, T., Hirschmann, M., et al. 2019, MNRAS, 489, 2702
Galbany, L., Anderson, J. P., Sánchez, S. F., et al. 2018, ApJ, 855, 107
Gallazzi, A., Brinchmann, J., Charlot, S., & White, S. D. M. 2008, MNRAS, 383, 1439
Gallazzi, A., Charlot, S., Brinchmann, J., White, S. D. M., & Tremonti, C. A. 2005, MNRAS, 362, 41
García-Benito, R., Zibetti, S., Sánchez, S. F., et al. 2015, A&A, 576, A135
García-Benito, R., González Delgado, R. M., Pérez, E., et al. 2017, A&A, 608, A27
García-Benito, R., González Delgado, R. M., Pérez, E., et al. 2019, A&A, 621, A120
Girardi, L., Bressan, A., Chiosi, C., Bertelli, G., & Nasi, E. 1996, A&AS, 117, 113
Girardi, L., Bressan, A., Bertelli, G., & Chiosi, C. 2000, A&AS, 141, 371
González Delgado, R. M., García-Benito, R., Pérez, E., et al. 2015, A&A, 581, A103
González Delgado, R. M., Cid Fernandes, R., Pérez, E., et al. 2016, A&A, 590, A44
González Delgado, R. M., Pérez, E., Cid Fernandes, R., et al. 2017, A&A, 607, A128
Häring, N., & Rix, H.-W. 2004, ApJ, 604, L89
Harrison, C. M. 2017, Nat. Astron., 1, 0165
Heckman, T. M., & Best, P. N. 2014, ARA&A, 52, 589
Hoversten, E. A., & Glazebrook, K. 2008, ApJ, 675, 163
Hubble, E. P. 1926, ApJ, 64, 321
Husemann, B., & Harrison, C. M. 2018, Nat. Astron., 2, 196
Husemann, B., Jahnke, K., Sánchez, S. F., et al. 2013, A&A, 549, A87
Kalinova, V., Colombo, D., Rosolowsky, E., et al. 2017a, MNRAS, 469, 2539
Kalinova, V., van de Ven, G., Lyubenova, M., et al. 2017b, MNRAS, 464, 1903
Kauffmann, G., & Haehnelt, M. 2000, MNRAS, 311, 576
Kauffmann, G., Heckman, T. M., White, S. D. M., et al. 2003, MNRAS, 341, 33
Kelz, A., Verheijen, M. A. W., Roth, M. M., et al. 2006, PASP, 118, 129
Kennicutt, R. C., & Evans, N. J. 2012, ARA&A, 50, 531
Kewley, L. J., Dopita, M. A., Sutherland, R. S., Heisler, C. A., & Trevena, J. 2001, ApJ, 556, 121
Kewley, L. J., Groves, B., Kauffmann, G., & Heckman, T. 2006, MNRAS, 372, 961
Kirkpatrick, A., Pope, A., Aretxaga, I., et al. 2014, ApJ, 796, 135
Lacerda, E. A. D., Cid Fernandes, R., Couto, G. S., et al. 2018, MNRAS, 474, 3727
Lacerda, E. A. D., Sánchez, S. F., Cid Fernandes, R., et al. 2020, MNRAS, 492, 3073
Le Borgne, J. F., Bruzual, G., Pelló, R., et al. 2003, A&A, 402, 433
Leung, G. Y. C., Leaman, R., van de Ven, G., et al. 2018, MNRAS, 477, 254
Lin, L., Belfiore, F., Pan, H.-A., et al. 2017, ApJ, 851, 18
Lin, L., Hsieh, B.-C., Pan, H.-A., et al. 2019, ApJ, 872, 50
López-Cobá, C., Sánchez, S. F., Bland-Hawthorn, J., et al. 2019, MNRAS, 482, 4032
López-Cobá, C., Sánchez, S. F., Anderson, J. P., et al. 2020, AJ, 159, 167
Lyubenova, M., Martín-Navarro, I., van de Ven, G., et al. 2016, MNRAS, 463, 3220
Mahoro, A., Pović, M., & Nkundabakura, P. 2017, MNRAS, 471, 3226
Marconi, A., & Hunt, L. K. 2003, ApJ, 589, L21
Martig, M., Bournaud, F., Teyssier, R., & Dekel, A. 2009, ApJ, 707, 250
Martins, L. P., González Delgado, R. M., Leitherer, C., Cerviño, M., & Hauschildt, P. 2005, MNRAS, 358, 49
McConnell, N. J., & Ma, C.-P. 2013, ApJ, 764, 184
McGaugh, S. S., Schombert, J. M., Bothun, G. D., & de Blok, W. J. G. 2000, ApJ, 533, L99
McNamara, B. R., Russell, H. R., Nulsen, P. E. J., et al. 2016, ApJ, 830, 79
Méndez-Abreu, J., Ruiz-Lara, T., Sánchez-Menguiano, L., et al. 2017, A&A, 598, A32
Nesvadba, N. P. H., Boulanger, F., Salomé, P., et al. 2010, A&A, 521, A65
Renzini, A., & Peng, Y.-J. 2015, ApJ, 801, L29
Roth, M. M., Kelz, A., Fechner, T., et al. 2005, PASP, 117, 620
Saintonge, A., Tacconi, L. J., Fabello, S., et al. 2012, ApJ, 758, 73
Saintonge, A., Catinella, B., Tacconi, L. J., et al. 2017, ApJS, 233, 22
Salim, S., Rich, R. M., Charlot, S., et al. 2007, ApJS, 173, 267
Salpeter, E. E. 1955, A&A, 121, 161
Sánchez, S. F. 2020, ARA&A, 58, 99
Sánchez, S. F., Kennicutt, R. C., Gil de Paz, A., et al. 2012, A&A, 538, A8
Sánchez, S. F., Rosales-Ortega, F. F., Jungwiert, B., et al. 2013, A&A, 554, A58
Sánchez, S. F., Rosales-Ortega, F. F., Iglesias-Páramo, J., et al. 2014, A&A, 563, A49
Sánchez, S. F., García-Benito, R., Zibetti, S., et al. 2016a, A&A, 594, A36
Sánchez, S. F., Pérez, E., Sánchez-Blázquez, P., et al. 2016b, Rev. Mexicana Astron. Astrofis., 52, 171
Sánchez, S. F., Pérez, E., Sánchez-Blázquez, P., et al. 2016c, Rev. Mexicana Astron. Astrofis., 52, 21
Sánchez, S. F., Avila-Reese, V., Hernandez-Toledo, H., et al. 2018, Rev. Mexicana Astron. Astrofis., 54, 217
Sánchez, S. F., Avila-Reese, V., Rodríguez-Puebla, A., et al. 2019, MNRAS, 482, 1557
Sánchez-Blázquez, P., Peletier, R. F., Jiménez-Vicente, J., et al. 2006, MNRAS, 371, 703
Sánchez-Menguiano, L., Sánchez, S. F., Pérez, I., et al. 2016, A&A, 587, A70
Sánchez-Menguiano, L., Sánchez, S. F., Pérez, I., et al. 2018, A&A, 609, A119
Sarzi, M., Shields, J. C., Schawinski, K., et al. 2010, MNRAS, 402, 2187
Schaerer, D., Charbonnel, C., Meynet, G., Maeder, A., & Schaller, G. 1993a, A&AS, 102, 339
Schaerer, D., Meynet, G., Maeder, A., & Schaller, G. 1993b, A&AS, 98, 523
Schaller, G., Schaerer, D., Meynet, G., & Maeder, A. 1992, A&AS, 96, 269
Schawinski, K., Thomas, D., Sarzi, M., et al. 2007, MNRAS, 382, 1415
Schawinski, K., Urry, C. M., Simmons, B. D., et al. 2014, MNRAS, 440, 889
Schaye, J., Crain, R. A., Bower, R. G., et al. 2015, MNRAS, 446, 521
Shin, J., Woo, J.-H., Chung, A., et al. 2019, ApJ, 881, 147
Silk, J. 2013, ApJ, 772, 112
Silk, J., & Rees, M. J. 1998, A&A, 331, L1
Singh, R., van de Ven, G., Jahnke, K., et al. 2013, A&A, 558, A43
Speagle, J. S., Steinhardt, C. L., Capak, P. L., & Silverman, J. D. 2014, ApJS, 214, 15
Stasińska, G., Vale Asari, N., Cid Fernandes, R., et al. 2008, MNRAS, 391, L29
Strateva, I., Ivezić, Ž., Knapp, G. R., et al. 2001, AJ, 122, 1861
Struve, C., Oosterloo, T., Sancisi, R., Morganti, R., & Emonts, B. H. C. 2010, A&A, 523, A75
Thorp, M. D., Ellison, S. L., Simard, L., Sánchez, S. F., & Antonio, B. 2019, MNRAS, 482, L55
Tukey, J. W. 1977, Exploratory data analysis (Addison-Wesley Publishing Company)
Valdes, F., Gupta, R., Rose, J. A., Singh, H. P., & Bell, D. J. 2004, ApJS, 152, 251
Vazdekis, A., Sánchez-Blázquez, P., Falcón-Barroso, J., et al. 2010, MNRAS, 404, 1639
Veilleux, S., & Osterbrock, D. E. 1987, ApJS, 63, 295
Verheijen, M. A. W., Bershady, M. A., Andersen, D. R., et al. 2004, Astron. Nachr., 325, 151
Vulcani, B., Fritz, J., Poggianti, B. M., et al. 2020, ApJ, 892, 146
Wagner, A. Y., Bicknell, G. V., Umemura, M., Sutherland, R. S., & Silk, J. 2016, Astrono. Nachr., 337, 167
Walcher, C. J., Wisotzki, L., Bekeraité, S., et al. 2014, A&A, 569, A1
Weiner, B. J., Willmer, C. N. A., Faber, S. M., et al. 2006, ApJ, 653, 1027
Whitaker, K. E., van Dokkum, P. G., Brammer, G., & Franx, M. 2012, ApJ, 754, L29
Williams, R. J., Quadri, R. F., Franx, M., van Dokkum, P., & Labbé, I. 2009, ApJ, 691, 1879
Young, J. S., & Scoville, N. Z. 1991, ARA&A, 29, 581
Zhu, L., van de Ven, G., van den Bosch, R., et al. 2018a, Nat. Astron., 2, 233
Zhu, L., van de Ven, G., Méndez-Abreu, J., & Obreja, A. 2018b, MNRAS, 479, 945
Zibetti, S., Gallazzi, A. R., Ascasibar, Y., et al. 2017, MNRAS, 468, 1902
Zubovas, K., Nayakshin, S., King, A., & Wilkinson, M. 2013, MNRAS, 433, 3079

Appendix A: Diagnostic maps and diagrams for all 238 CALIFA galaxies

The resolved $W_{H\alpha}$ maps, $W_{H\alpha}$ profiles, BPT maps, and BPT diagrams for the full sample of 238 CALIFA galaxies are available at https://doi.org/10.5281/zenodo.4529149.

Appendix B: Tables with properties of the 238 CALIFA galaxies

In Tables B.1 and B.2, we list the main properties of the 238 (E1−Sdm) CALIFA galaxies, presented in this work.

Table B.1. Properties of the 238 (E1-Sdm) CALIFA galaxies.

Galaxy	D Mpc	Re arcsec	log M_* $M_\odot$	log SFR $M_\odot$ yr^{-1}	Δ SFR $M_\odot$ yr^{-1}	Type	Bar	QS	flag-QS	NA	flag-NA
(1)	(2)	(3)	(4)	(5)	(6)	(7)	(8)	(9)	(10)	(11)	(12)
IC0480	61.7	14.0	9.988	0.145	−0.016	Sc	AB	SF	1	nonA	S
IC0540	26.1	12.1	9.736	−0.903	−0.869	Sab	AB	MX	1	sAGN	S
IC0674	103.4	9.2	10.997	−0.096	−1.033	Sab	B	MX	2	nonA	S
IC0944	95.8	13.6	11.108	0.026	−0.996	Sab	A	MX	1	nonA	S
IC1079	119.3	18.2	11.252	−0.628	−1.762	E4	A	nR	2	nonA	S
IC1151	31.0	19.9	9.521	0.006	0.206	Scd	B	SF	1	nonA	S
IC1256	67.0	10.1	10.397	0.157	−0.319	Sb	AB	SF	1	nonA	S
IC1528	53.3	16.0	10.134	0.428	0.155	Sbc	AB	SF	1	nonA	S
IC1652	72.9	8.3	10.502	−1.479	−2.035	S0a	A	fR	1	nonA	S
IC1755	109.9	16.4	10.977	−0.507	−1.429	Sb	A	MX	1	nonA	S
IC2101	60.7	15.8	10.164	0.425	0.130	Scd	AB	SF	1	nonA	S
IC2247	57.7	15.2	10.429	0.154	−0.345	Sab	A	SF	1	sAGN	S
IC2487	58.3	15.8	10.326	0.202	−0.219	Sc	AB	SF	1	nonA	S
IC4566	81.0	12.7	10.779	−0.025	−0.794	Sb	B	MX	1	nonA	S
IC5309	59.6	15.9	10.109	0.164	−0.089	Sc	AB	SF	2	nonA	S
IC5376	71.5	11.1	10.584	−0.254	−0.873	Sb	A	cQ	1	nonA	S
MCG-01-54-016	42.1	16.8	9.156	−0.528	−0.048	Scd	A	SF	1	nonA	S
MCG-02-02-030	48.9	12.4	10.291	−0.103	−0.497	Sb	AB	QnR	1	sAGN	U
MCG-02-02-040	49.8	16.1	9.952	0.108	−0.025	Scd	AB	SF	1	nonA	S
MCG-02-03-015	79.8	12.7	–	–	–	Sab	AB	SF	3	nonA	S
MCG-02-51-004	79.3	11.6	10.650	0.402	−0.268	Sb	A	SF	1	nonA	S
NGC 0001	64.7	11.7	10.691	0.494	−0.207	Sbc	A	SF	1	nonA	S
NGC 0023	64.9	7.8	10.935	0.983	0.094	Sb	B	SF	1	nonA	S
NGC 0155	85.8	9.2	10.884	−1.809	−2.659	E1	A	fR	1	nonA	S
NGC 0160	74.0	16.8	11.047	0.050	−0.926	Sa	A	cQ	2	nonA	S
NGC 0171	53.9	18.0	10.641	−0.228	−0.890	Sb	B	cQ	1	nonA	S
NGC 0177	52.7	16.2	–	–	–	Sab	A	QnR	2	nonA	S
NGC 0192	57.9	14.2	10.750	0.348	−0.399	Sab	AB	MX	1	nonA	S
NGC 0214	64.2	14.8	10.801	0.715	−0.071	Sbc	AB	SF	1	wAGN	S
NGC 0216	21.4	10.9	9.185	−0.404	0.054	Sd	A	SF	1	nonA	S
NGC 0217	55.2	19.2	10.832	−0.258	−1.068	Sa	A	MX	1	nonA	S
NGC 0237	58.4	10.1	10.195	0.507	0.187	Sc	B	SF	1	nonA	S
NGC 0257	73.7	16.2	10.842	0.941	0.124	Sc	A	SF	1	nonA	S
NGC 0429	78.0	6.7	10.736	−1.448	−2.184	Sa	A	fR	1	nonA	S
NGC 0444	68.3	15.2	9.794	0.090	0.080	Scd	A	SF	1	nonA	S
NGC 0499	62.3	9.2	11.240	−1.140	−2.265	E5	A	fR	1	nonA	S
NGC 0504	59.9	6.8	10.587	−1.410	−2.032	S0	A	fR	1	nonA	S
NGC 0517	59.6	5.8	10.644	−1.509	−2.175	S0	A	fR	1	nonA	S
NGC 0528	67.8	8.2	10.932	−0.970	−1.857	S0	A	nR	1	nonA	S
NGC 0529	68.1	9.9	11.079	−0.977	−1.977	E4	A	fR	1	nonA	S

Notes. Columns list: (1) Galaxy identifier (NED); (2) Galactocentric galaxy distance in Mpc (NED); (3) Effective radius of the galaxy in arcseconds, measured from SDSS images via growth curve analysis using elliptical apertures (Sanchez et al., in prep.); (4) Stellar mass, adopting Chabrier IMF in $M_\odot$ (Sect. 2.3); (5) SFR of the galaxies in $M_\odot$ yr^{-1} (Sect. 2.3); (6) SFR distance, measured from the SFMS in $M_\odot$ yr^{-1} (Sect. 6.1); (7) Hubble type based on by-eye morphological classification from Walcher et al. (2014); (8) Bar class based on by-eye morphological classification from Walcher et al. (2014), where A–non-barred galaxy, B–barred galaxy and AB – unsure bar in the galaxy (Sect. 5.1); (9) Quenching stages (QS) of the 238 CALIFA galaxies, where SF – Star-forming, QnR – quiescent-nuclear-ring; cQ - centrally quiescent; MX – mixed; nR – nearly retired and fR – fully retired (Sect. 3); (10) Reliability of the QS classification, where 1 – sure class , 2 – unsure class due to complex structure of the galaxy, 3 – unsure class due to poor data (Sect. 3.3). (11) Nuclear activity groups for our sample, where nonA – non-active galaxy, wAGN–weak AGN and sAGN – strong AGN (Sect. 3.2). (12) Reliability of the NA classification, where S: sure class based on the information of the three BPT diagrams and U: unsure class based on the information of two from the three BPT diagrams (Sect. 3.3).

Table B.1. continued.

Galaxy	D	Re	log M_*	log SFR	Δ SFR	Type	Bar	QS	flag-QS	NA	flag-NA
	Mpc	arcsec	$M_\odot$	$M_\odot$ yr^{-1}	$M_\odot$ yr^{-1}						
(1)	(2)	(3)	(4)	(5)	(6)	(7)	(8)	(9)	(10)	(11)	(12)
NGC 0551	73.2	15.1	10.565	0.200	−0.404	Sbc	AB	QnR	1	nonA	S
NGC 0681	24.3	16.6	10.160	−0.245	−0.537	Sa	AB	MX	2	nonA	S
NGC 0741	77.0	15.4	11.434	−0.839	−2.113	E1	A	nR	1	nonA	S
NGC 0755	22.6	17.8	9.300	−0.298	0.072	Scd	B	SF	1	nonA	S
NGC 0768	96.7	15.2	10.579	0.450	−0.165	Sc	B	SF	1	nonA	S
NGC 0774	64.4	7.4	10.763	−0.992	−1.749	S0	A	nR	1	nonA	S
NGC 0776	68.8	13.2	10.803	0.382	−0.406	Sb	B	SF	1	nonA	S
NGC 0781	48.7	7.2	–	–	–	Sa	A	fR	3	nonA	S
NGC 0810	106.0	10.3	11.357	−0.350	−1.564	E5	A	nR	2	nonA	S
NGC 0932	56.9	14.0	10.957	−0.454	−1.360	S0a	A	nR	2	nonA	S
NGC 1056	22.4	8.0	10.017	0.093	−0.090	Sa	A	SF	1	nonA	S
NGC 1060	72.5	13.0	11.472	−0.654	−1.957	E3	A	fR	1	nonA	S
NGC 1167	69.1	13.4	11.231	−0.320	−1.437	S0	A	nR	1	sAGN	U
NGC 1349	90.2	11.1	11.112	−0.128	−1.154	E6	A	MX	2	nonA	S
NGC 1542	50.3	8.9	10.314	0.054	−0.357	Sab	AB	MX	1	nonA	S
NGC 1645	65.9	12.2	10.764	−0.481	−1.239	S0a	B	MX	1	nonA	S
NGC 1677	36.5	15.2	9.467	−0.195	0.046	Scd	AB	SF	1	nonA	S
NGC 2253	50.2	14.0	10.518	0.567	−0.001	Sbc	B	SF	1	nonA	S
NGC 2347	61.9	12.0	10.681	0.653	−0.041	Sbc	AB	SF	1	nonA	S
NGC 2410	63.7	16.1	10.767	0.267	−0.494	Sb	AB	SF	1	sAGN	S
NGC 2449	66.3	11.9	10.854	−0.013	−0.840	Sab	AB	MX	1	nonA	S
NGC 2476	51.0	6.9	10.673	−0.771	−1.458	E6	A	fR	1	nonA	S
NGC 2481	28.6	14.8	10.542	−1.515	−2.102	S0	A	MX	1	nonA	S
NGC 2486	62.8	19.4	–	–	–	Sab	B	MX	1	nonA	S
NGC 2553	63.5	8.6	10.591	−1.038	−1.662	Sb	AB	fR	1	nonA	S
NGC 2554	56.0	15.3	11.032	−0.418	−1.382	S0a	A	nR	1	wAGN	S
NGC 2592	26.2	6.8	10.234	−2.309	−2.659	E4	A	fR	1	nonA	S
NGC 2604	27.8	18.0	9.343	−0.226	0.111	Sd	B	SF	1	nonA	S
NGC 2639	46.1	10.9	10.853	−0.191	−1.018	Sa	A	MX	1	sAGN	S
NGC 2730	51.1	18.2	9.931	0.347	0.231	Scd	B	SF	1	nonA	S
NGC 2880	22.4	10.0	10.324	−2.292	−2.710	E7	AB	fR	1	nonA	S
NGC 2906	27.6	12.2	10.261	−0.098	−0.469	Sbc	A	cQ	2	nonA	S
NGC 2916	50.0	18.7	10.455	0.314	−0.206	Sbc	A	cQ	1	nonA	S
NGC 2918	93.1	7.3	10.986	−1.247	−2.176	E6	A	fR	1	nonA	S
NGC 3057	22.9	18.5	8.775	−0.806	−0.033	Sdm	B	SF	1	nonA	S
NGC 3106	84.5	11.8	11.088	−0.144	−1.151	Sab	A	MX	2	nonA	S
NGC 3160	94.7	11.0	10.706	−0.508	−1.220	Sab	AB	MX	1	sAGN	S
NGC 3300	40.9	10.1	10.484	−1.560	−2.102	S0a	B	fR	1	nonA	S
NGC 3381	22.1	16.2	9.365	−0.143	0.177	Sd	B	SF	1	nonA	S
NGC 3615	90.9	6.3	11.216	−0.837	−1.943	E5	A	fR	1	nonA	S
NGC 3811	43.2	15.3	10.304	0.202	−0.201	Sbc	B	QnR	1	nonA	S
NGC 3815	50.4	10.0	10.406	0.649	0.167	Sbc	A	SF	1	nonA	S
NGC 3994	42.3	5.7	10.314	0.598	0.187	Sbc	AB	SF	1	nonA	S
NGC 4003	88.7	8.7	10.959	−0.156	−1.063	S0a	B	MX	2	nonA	S
NGC 4047	47.5	12.9	10.506	0.620	0.060	Sbc	A	SF	1	nonA	S
NGC 4149	43.1	11.7	10.202	−0.373	−0.698	Sa	AB	MX	1	nonA	S
NGC 4185	53.4	22.4	10.555	−0.030	−0.626	Sbc	AB	cQ	1	nonA	S
NGC 4210	39.0	19.2	10.180	−0.033	−0.341	Sb	B	cQ	1	nonA	S
NGC 4470	31.1	12.0	9.781	0.202	0.201	Sc	A	SF	1	nonA	S
NGC 4644	69.0	13.4	10.410	−0.024	−0.510	Sb	A	cQ	1	nonA	S
NGC 4711	56.1	12.5	10.511	0.672	0.109	Sbc	A	SF	1	nonA	S
NGC 4816	94.9	10.3	11.067	−0.605	−1.596	E1	A	nR	1	nonA	S
NGC 4956	65.6	6.8	10.873	−0.830	−1.672	E1	A	fR	1	nonA	S
NGC 4961	35.0	11.1	9.478	0.070	0.302	Scd	B	SF	1	nonA	S
NGC 5000	77.1	14.5	10.667	0.233	−0.450	Sbc	B	QnR	2	nonA	S
NGC 5029	120.9	9.5	11.423	−0.474	−1.740	E6	A	nR	1	nonA	S
NGC 5056	77.0	13.2	–	–	–	Sc	AB	SF	1	nonA	S

Table B.1. continued.

Galaxy	D	Re	log M_*	log SFR	Δ SFR	Type	Bar	QS	flag-QS	NA	flag-NA
	Mpc	arcsec	$M_\odot$	$M_\odot$ yr^{-1}	$M_\odot$ yr^{-1}						
(1)	(2)	(3)	(4)	(5)	(6)	(7)	(8)	(9)	(10)	(11)	(12)
NGC 5218	41.9	16.1	10.445	0.083	−0.429	Sab	B	MX	1	nonA	S
NGC 5378	42.7	16.6	10.341	−0.976	−1.408	Sb	B	MX	2	nonA	S
NGC 5480	27.0	15.1	9.716	0.172	0.221	Scd	A	SF	1	nonA	S
NGC 5485	28.1	12.8	10.530	−1.780	−2.358	E5	A	fR	1	nonA	S
NGC 5520	27.3	11.0	9.691	−0.041	0.027	Sbc	A	SF	1	nonA	S
NGC 5614	54.4	12.3	11.109	−0.098	−1.122	Sa	A	nR	1	wAGN	S
NGC 5630	37.7	13.3	9.513	0.284	0.490	Sdm	B	SF	1	nonA	S
NGC 5633	33.5	11.2	10.012	0.325	0.146	Sbc	A	SF	1	nonA	S
NGC 5657	54.5	10.7	10.260	0.190	−0.179	Sbc	B	SF	1	nonA	S
NGC 5682	32.8	25.2	9.109	−0.483	0.034	Scd	B	SF	1	nonA	S
NGC 5720	108.4	12.4	10.947	0.120	−0.779	Sbc	B	cQ	1	nonA	S
NGC 5732	52.7	13.2	9.726	0.026	0.067	Sbc	A	SF	1	nonA	S
NGC 5784	75.1	8.6	11.054	−0.068	−1.048	S0	A	nR	1	nonA	S
NGC 5876	46.9	11.6	10.654	−0.833	−1.506	S0a	B	nR	2	nonA	S
NGC 5888	121.3	12.0	11.273	0.360	−0.789	Sb	B	cQ	2	nonA	S
NGC 5908	47.3	16.2	10.941	−0.051	−0.945	Sa	A	MX	1	nonA	S
NGC 5971	61.2	9.8	10.079	−0.421	−0.651	Sb	AB	MX	2	wAGN	S
NGC 5980	57.1	13.2	10.666	0.848	0.166	Sbc	A	SF	1	nonA	S
NGC 5987	43.5	19.7	10.753	−0.796	−1.545	Sa	A	nR	1	nonA	S
NGC 6020	60.4	7.3	10.808	−1.451	−2.242	E4	A	fR	1	nonA	S
NGC 6021	66.2	5.9	10.896	−1.282	−2.142	E5	A	fR	1	nonA	S
NGC 6032	60.1	14.8	10.281	−0.297	−0.683	Sbc	B	MX	2	nonA	S
NGC 6060	62.3	22.3	10.795	0.676	−0.106	Sb	A	SF	1	nonA	S
NGC 6063	40.0	17.9	9.924	−0.372	−0.483	Sbc	A	SF	1	nonA	S
NGC 6081	72.0	10.0	10.935	−0.546	−1.435	S0a	A	nR	1	sAGN	U
NGC 6125	68.6	8.0	11.202	−1.426	−2.521	E1	A	fR	1	nonA	S
NGC 6132	69.2	14.2	10.099	0.325	0.080	Sbc	A	SF	1	nonA	S
NGC 6146	123.0	7.9	11.463	−0.767	−2.063	E5	A	nR	1	wAGN	U
NGC 6150	121.6	7.2	11.252	−0.744	−1.878	E7	A	fR	1	nonA	S
NGC 6168	36.1	18.1	9.596	−0.031	0.111	Sc	AB	SF	1	nonA	S
NGC 6173	122.5	13.9	11.681	−0.576	−2.040	E6	A	nR	2	nonA	S
NGC 6186	41.9	11.9	10.454	0.183	−0.336	Sb	B	MX	1	nonA	S
NGC 6278	40.7	8.4	10.676	−1.970	−2.660	S0a	AB	fR	1	nonA	S
NGC 6301	116.8	21.5	10.870	0.524	−0.315	Sbc	A	SF	1	nonA	S
NGC 6310	49.5	15.3	10.451	−0.353	−0.870	Sb	A	cQ	1	nonA	S
NGC 6314	92.9	9.4	10.921	−0.195	−1.073	Sab	A	nR	1	nonA	S
NGC 6478	95.6	15.5	10.986	0.796	−0.133	Sc	A	SF	1	nonA	S
NGC 6497	87.2	12.3	10.885	−0.050	−0.901	Sab	B	cQ	1	nonA	S
NGC 6515	96.7	10.8	11.086	−0.945	−1.951	E3	A	nR	1	nonA	S
NGC 6762	43.0	10.3	10.205	−1.714	−2.042	Sab	A	nR	1	wAGN	S
NGC 6941	87.2	16.6	10.982	0.072	−0.853	Sb	B	QnR	1	nonA	S
NGC 6945	53.9	8.8	9.385	−2.882	−2.578	S0	B	fR	1	nonA	S
NGC 6978	84.5	14.9	10.814	0.198	−0.598	Sb	AB	MX	2	nonA	S
NGC 7025	70.8	13.0	11.242	−0.629	−1.754	S0a	A	nR	1	nonA	S
NGC 7047	81.7	17.3	10.721	0.324	−0.401	Sbc	B	cQ	1	nonA	S
NGC 7194	112.7	3.6	11.345	−1.158	−2.363	E3	A	fR	1	nonA	S
NGC 7311	64.3	8.6	11.117	0.105	−0.925	Sa	A	cQ	1	nonA	S
NGC 7321	100.5	13.0	11.028	0.495	−0.466	Sbc	B	QnR	1	wAGN	U
NGC 7364	68.5	8.0	10.706	0.483	−0.230	Sab	A	SF	1	nonA	S
NGC 7466	105.5	12.7	10.709	0.455	−0.260	Sbc	A	SF	1	sAGN	S
NGC 7489	88.0	16.2	10.493	0.748	0.199	Sbc	A	SF	1	nonA	S
NGC 7549	67.3	19.1	10.510	0.780	0.218	Sbc	B	SF	2	nonA	S
NGC 7550	71.9	11.2	11.157	−1.067	−2.128	E4	A	nR	1	wAGN	U
NGC 7562	51.4	10.5	11.187	−0.979	−2.063	E4	A	fR	1	nonA	S
NGC 7563	59.4	7.5	11.026	−1.391	−2.350	Sa	B	fR	1	nonA	S
NGC 7591	69.9	11.7	10.731	0.703	−0.030	Sbc	B	SF	1	nonA	S

Table B.1. continued.

Galaxy	D	Re	log M_*	log SFR	Δ SFR	Type	Bar	QS	flag-QS	NA	flag-NA
	Mpc	arcsec	$M_\odot$	$M_\odot$ yr^{-1}	$M_\odot$ yr^{-1}						
(1)	(2)	(3)	(4)	(5)	(6)	(7)	(8)	(9)	(10)	(11)	(12)
NGC 7608	50.1	12.4	9.946	0.043	−0.085	Sbc	A	SF	1	nonA	S
NGC 7611	46.6	9.0	10.652	−0.999	−1.671	S0	A	fR	1	nonA	S
NGC 7619	53.6	11.2	11.267	−1.075	−2.220	E3	A	fR	1	nonA	S
NGC 7623	53.3	6.8	10.732	−1.353	−2.087	S0	A	fR	1	nonA	S
NGC 7625	24.7	10.7	9.963	0.210	0.069	Sa	A	SF	2	nonA	S
NGC 7631	53.5	13.8	10.507	0.009	−0.551	Sb	A	QnR	1	nonA	S
NGC 7653	60.7	11.8	10.512	0.471	−0.093	Sb	A	cQ	1	nonA	S
NGC 7671	58.7	6.4	10.798	−2.010	−2.794	S0	A	fR	1	nonA	S
NGC 7683	53.2	9.6	10.972	−1.129	−2.048	S0	A	fR	1	nonA	S
NGC 7711	57.8	12.0	10.835	−1.047	−1.860	E7	A	MX	2	nonA	S
NGC 7716	37.0	12.3	10.410	−0.231	−0.716	Sb	A	cQ	1	nonA	S
NGC 7722	57.4	12.9	10.934	0.085	−0.804	Sab	A	MX	2	nonA	S
NGC 7738	94.2	13.1	11.031	0.716	−0.247	Sb	B	MX	1	nonA	S
NGC 7787	92.8	11.2	10.573	0.215	−0.396	Sab	AB	QnR	1	nonA	S
NGC 7819	70.4	12.4	10.068	0.326	0.104	Sc	A	SF	1	nonA	S
NGC 7824	85.7	9.6	11.045	−0.224	−1.198	Sab	A	nR	1	sAGN	U
UGC00005	101.0	13.0	10.843	0.795	−0.023	Sbc	A	SF	1	sAGN	U
UGC00029	122.7	10.4	–	–	–	E1	A	nR	1	nonA	S
UGC00036	87.9	11.2	10.897	−0.083	−0.943	Sab	AB	MX	1	nonA	S
UGC00148	59.7	4.5	10.148	0.831	0.547	Sc	A	SF	1	nonA	S
UGC00312	61.4	15.7	9.851	0.439	0.384	Sd	B	SF	1	nonA	S
UGC00809	59.6	11.7	9.586	−0.107	0.042	Scd	A	SF	1	nonA	S
UGC00987	65.8	9.8	10.724	−0.303	−1.030	Sa	AB	SF	1	sAGN	S
UGC01057	88.7	10.8	10.258	0.328	−0.040	Sc	AB	SF	1	nonA	S
UGC01271	70.8	6.1	10.772	−0.724	−1.487	S0a	B	fR	1	nonA	S
UGC02222	70.6	10.3	10.696	−1.237	−1.942	S0a	AB	fR	1	nonA	S
UGC02229	100.5	16.3	10.918	−0.544	−1.420	S0a	A	nR	1	nonA	S
UGC02403	56.8	12.3	10.395	0.153	−0.320	Sb	B	SF	1	nonA	S
UGC03253	58.8	19.2	10.360	−0.181	−0.628	Sb	B	QnR	1	nonA	S
UGC03539	46.7	19.2	9.654	−0.072	0.025	Sc	AB	SF	1	nonA	S
UGC03995	64.4	18.0	10.933	−0.003	−0.891	Sb	B	QnR	2	sAGN	S
UGC04029	60.1	17.9	10.250	0.148	−0.214	Sc	AB	SF	1	nonA	S
UGC04132	71.0	14.3	10.748	0.893	0.147	Sbc	AB	SF	1	nonA	S
UGC04145	62.0	8.6	10.468	0.509	−0.021	Sa	AB	MX	1	sAGN	S
UGC04197	61.1	15.6	10.497	−0.342	−0.894	Sab	AB	cQ	1	nonA	S
UGC04280	48.8	9.9	10.190	−0.318	−0.634	Sb	AB	SF	1	nonA	S
UGC04308	47.8	20.6	10.021	0.191	0.006	Sc	B	SF	1	nonA	S
UGC05108	110.2	12.9	10.927	0.164	−0.719	Sb	B	QnR	1	nonA	S
UGC05113	94.7	8.1	10.913	−1.213	−2.085	S0a	AB	nR	1	nonA	S
UGC05598	76.2	11.9	10.066	0.219	−0.001	Sb	A	SF	1	nonA	S
UGC05771	101.6	6.9	11.141	−0.318	−1.366	E6	A	nR	1	nonA	S
UGC05990	21.3	7.7	–	–	–	Sc	A	SF	1	nonA	S
UGC06036	89.0	10.2	11.039	−0.324	−1.293	Sa	A	MX	1	nonA	S
UGC06312	85.2	11.5	10.793	−0.161	−0.941	Sab	A	MX	1	nonA	S
UGC07012	42.1	10.4	9.266	−0.175	0.220	Scd	AB	SF	1	nonA	S
UGC07145	91.3	12.4	10.343	0.059	−0.374	Sbc	A	SF	1	nonA	S
UGC08107	115.0	15.4	11.059	0.834	−0.151	Sa	A	SF	1	nonA	S
UGC08231	35.2	13.9	9.035	−0.216	0.358	Sd	AB	SF	1	nonA	S
UGC08234	112.6	4.7	11.040	0.070	−0.900	S0	A	fR	1	nonA	S
UGC08733	33.2	19.8	9.072	−0.788	−0.243	Sdm	B	SF	1	nonA	S
UGC08778	45.8	9.8	9.994	−0.594	−0.759	Sb	A	MX	1	nonA	S
UGC08781	104.3	10.9	10.978	−0.138	−1.060	Sb	B	cQ	1	nonA	S
UGC09476	46.2	17.2	10.032	0.195	0.001	Sbc	A	SF	1	nonA	S
UGC09537	122.1	16.5	11.054	0.212	−0.770	Sb	A	cQ	1	nonA	S
UGC09542	76.4	15.0	10.185	0.227	−0.085	Sc	A	SF	1	nonA	S
UGC09665	36.8	14.5	9.798	0.069	0.055	Sb	A	SF	1	nonA	S
UGC09873	78.8	16.3	9.905	−0.076	−0.172	Sb	A	SF	1	nonA	S

Table B.1. continued.

Galaxy	D	Re	log M_*	log SFR	Δ SFR	Type	Bar	QS	flag-QS	NA	flag-NA
	Mpc	arcsec	$M_\odot$	$M_\odot$ yr^{-1}	$M_\odot$ yr^{-1}						
(1)	(2)	(3)	(4)	(5)	(6)	(7)	(8)	(9)	(10)	(11)	(12)
UGC09892	79.5	13.0	10.137	0.165	−0.110	Sbc	A	SF	1	nonA	S
UGC10097	83.8	7.8	11.242	−0.973	−2.099	E5	A	nR	1	nonA	S
UGC10123	53.8	10.6	10.306	0.328	−0.077	Sab	A	SF	1	nonA	S
UGC10205	91.6	14.6	10.952	0.353	−0.550	S0a	A	nR	1	nonA	S
UGC10257	54.5	20.1	10.511	0.858	0.294	Sbc	A	SF	1	nonA	S
UGC10331	63.7	17.3	9.840	0.184	0.138	Sc	AB	SF	1	nonA	S
UGC10337	121.1	11.3	10.967	0.540	−0.375	Sb	A	cQ	1	nonA	S
UGC10384	69.3	8.6	10.234	0.639	0.290	Sb	A	SF	1	nonA	S
UGC10388	64.9	6.7	10.473	−0.718	−1.252	Sa	AB	MX	2	nonA	S
UGC10650	42.5	11.3	9.170	−0.218	0.252	Scd	A	SF	1	nonA	S
UGC10693	116.9	10.2	11.272	−0.655	−1.804	E7	AB	fR	1	nonA	S
UGC10695	116.5	11.7	11.190	−0.733	−1.819	E5	A	nR	1	nonA	S
UGC10710	117.3	13.9	10.885	1.275	0.424	Sb	A	SF	1	nonA	S
UGC10796	44.8	11.4	9.199	−0.259	0.188	Scd	AB	SF	1	nonA	S
UGC10811	122.5	10.7	10.955	0.468	−0.437	Sb	B	cQ	1	nonA	S
UGC10905	109.7	17.6	11.277	−0.342	−1.495	S0a	A	nR	1	nonA	S
UGC10972	66.1	15.0	10.329	−0.219	−0.642	Sbc	A	cQ	1	nonA	S
UGC11228	81.9	6.2	10.962	−1.303	−2.214	S0	B	nR	1	nonA	S
UGC11717	89.1	11.6	10.824	0.802	−0.001	Sab	A	MX	1	sAGN	U
UGC12054	30.6	10.0	8.993	−0.557	0.048	Sc	A	SF	1	nonA	S
UGC12127	116.2	16.5	11.339	−0.702	−1.903	E1	A	nR	1	nonA	S
UGC12185	93.9	16.5	10.693	−0.128	−0.831	Sb	B	cQ	1	nonA	S
UGC12274	107.7	20.6	11.072	−0.340	−1.336	Sa	A	nR	1	nonA	S
UGC12308	32.9	20.3	8.916	−0.571	0.094	Scd	A	SF	1	nonA	S
UGC12518	40.2	11.8	10.374	−0.490	−0.948	Sb	A	MX	2	nonA	S
UGC12519	62.3	12.5	10.124	0.325	0.060	Sc	AB	SF	1	nonA	S
UGC12723	76.9	5.8	9.628	−0.144	−0.027	Sc	A	SF	1	nonA	S
UGC12857	35.5	13.8	9.578	−0.213	−0.058	Sbc	A	SF	1	nonA	S

Table B.2. Median values of galaxy properties from the box-and-whisker diagrams in Fig. 9 (see Sects. 2 and 5).

QS	B/D	log L_r^{tot}	R_e	log μ_*	log M_*^{tot}	log τ	log Z	log SFR	λ_{R_e}	$V_{c,max}$	log M_{dyn}^{tot}	f_d
		$[L_\odot]$	[kpc]	$[M_\odot/pc^2]$	$[M_\odot]$	[yr]	$[Z_\odot]$	$[M_\odot$ yr$^{-1}]$		[km s^{-1}]		
(1)	(2)	(3)	(4)	(5)	(6)	(7)	(8)	(9)	(10)	(11)	(12)	(13)
SF-nonA	0.08	10.03	3.41	2.38	10.07	8.80	−0.24	0.20	0.60	171.85	10.77	0.80
QnR-nonA	0.09	10.26	5.35	2.67	10.57	9.45	0.04	0.18	0.70	205.83	10.95	0.64
cQ-nonA	0.11	10.51	4.81	2.83	10.64	9.52	0.12	−0.03	0.66	237.26	11.18	0.65
MX-nonA	0.30	10.50	3.89	3.01	10.80	9.65	0.08	−0.15	0.58	245.28	11.25	0.66
nR-nonA	0.58	10.79	4.89	3.19	11.07	9.81	0.19	−0.63	0.29	343.61	11.62	0.68
fR-nonA	0.69	10.47	2.23	3.39	10.81	9.77	0.21	−1.25	0.39	326.74	11.22	0.64

Notes. Columns list: (1) QS of non-active (nonA) galaxies, where: SF – Star-forming, QnR – quiescent-nuclear-ring; cQ - centrally quiescent; MX – mixed; nR – nearly retired and fR – fully retired (Sect. 3); (2) The median bulge-to-disc ratios for a given EL class; (3) The median value of the total r-band luminosity for a given EL class; (4) The median values of the effective radius for a given EL class; (5) The median stellar mass surface density for a given EL class; (6) The median total stellar mass of the galaxies for a given EL class; (7) The median value of the galaxy age for a given EL class; (8) The median value of galaxy metallicity for a given EL class; (9) The median value of star formation rate for a given EL class; (10) The median value of the specific angular momentum within one effective radius for a given EL class; (11) The median value of the maximum circular velocity for a given EL class; (12) The median value of the total dynamical mass for a given EL class; (13) The median value of mass discrepancy factor, $f_d = 1 - (M_*^{tot}/M_{dyn}^{tot})$, for a given EL class; see text in Sects. 2 and 5 for more details.